WF - Research & Innovation,
Kelowna, British Columbia, Canada 2023

Seismic Hazard and Ground Motion Selection for Response History Analysis based on the National Building Code of Canada 2020

Dr. Solomon Tesfamariam, P.Eng.
(Professor, UBC Okanagan Campus, BC, Canada)

Dr. Prakash S Badal
(Postdoctoral Fellow, UBC Okanagan Campus, BC, Canada)

Dr. Katsuichiro Goda
(Associate Professor, Western University, ON, Canada)

May 2023

THE UNIVERSITY OF BRITISH COLUMBIA
FACULTY OF APPLIED SCIENCE, SCHOOL OF ENGINEERING

How to cite this report:

Tesfamariam, Solomon, Badal, Prakash Singh, & Goda, Katsuichiro (2023). *Seismic Hazard and Ground Motion Selection for Response History Analysis based on the National Building Code of Canada 2020*. UBC Faculty Research and Publications. https://dx.doi.org/10.14288/1.0431445

Disclaimers

This report includes seismic hazard calculation and ground motion selection for any location in Canada. The calculations are based on the seismic source modeling developed by NRCan. Assessment methods with different assumptions and inputs for seismic hazard models are possible. Such methods and procedures may result in different estimates of seismic hazards. The report is attempted to closely represent the sixth seismic hazard model presented in NBC 2020. The report has no intention of promoting or endorsing any particular proprietary software. The authors have taken reasonable actions and due diligence to ensure the accuracy of the information provided in this report; however, THE AUTHORS, UNIVERSITY OF BRITISH COLUMBIA, OR OTHER CONTRIBUTORS ASSUME NO LIABILITY FOR ANY DIRECT OR INDIRECT DAMAGE, INJURY, LOSS OR EXPENSE THAT MAY BE INCURRED OR SUFFERED AS A RESULT OF THE USE OF THIS REPORT INCLUDING WITHOUT LIMITATION PRODUCTS, BUILDING TECHNIQUES OR PRACTICES. The authors do not guarantee the completeness of the information published in this report. Users of this report agree to use the information in this report (analysis suggestions, design procedures, detailing, etc.) at their own risk. We will not be liable for any errors, inaccuracies, omissions or damages arising from the use of the information presented in this report, nor any action taken in reliance to the presented information. Seismic hazard estimates, underlying assumptions, and models are subject to change based on new data, information, or research. Rather than relying on this report, it is advisable to: (a) regularly consult up-to-date technical publications by NRCan and the Canadian Commission on Building and Fire Codes, (b) seek specific information on the use of hazard models from the subject experts with appropriate qualifications and experience, and (c) review and comply with the specific requirements of the applicable building codes.

Acknowledgments

Development of the seismic hazard modules developed in this project was supported through the BC Forestry Innovation Investment's (FII) Wood First Program. The financial support through NSERC Alliance is acknowledged.

Contents

Chapter 1

Introduction

Canada is a vast country with diverse seismic sources. While crustal and subduction earthquakes contribute to the seismicity of western Canada, stable continental intraplate earthquakes are significant contributors in the east. National Resources Canada (NRCan) is entrusted with developing seismic hazard estimates. Beginning with the first model in 1953, six national models have been created for this purpose. NRCan developed the latest sixth seismic hazard model (SHM6) for the seismic hazard estimates in the National Building Code of Canada (NBCC, Canadian Commission on Building and Fire Codes, 2022).

The seismic hazard assessment and resulting estimates of ground shaking levels are useful for structural engineers in designing buildings, bridges, dams, and several other types of infrastructure. A detailed understanding of seismicity is often required for research and development, and planning purposes. Development of design standards and estimating losses in the aftermath of an earthquake are examples. As a part of these detailed studies, seismic fragility is developed through nonlinear dynamic analysis. It is crucial to select a set of ground motion records representative of the location of interest (Tesfamariam and Goda, 2015; Goda, 2019; Tesfamariam et al., 2021; Odikamnoro et al., 2022).

Through Forest Innovation Investment's (FII) Wood First Program and NSERC (Natural Science and Engineering Research Council of Canada) grants, a team of researchers from The University of British Columbia (UBC) has built automated tools for the rigorous ground motion selection and further post-processing of ground motion records leveraging SHM6. This report presents the procedure and a summary of

findings from the project.

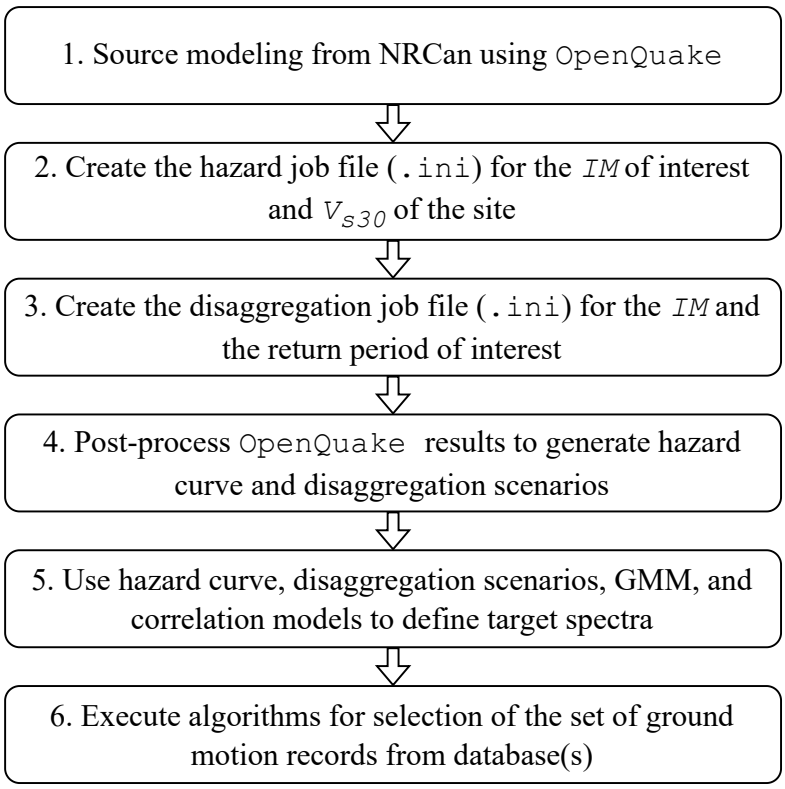

IM- Intensity Measure; V_{s30}- average shear-wave velocity in the uppermost 30 m (in m/s); GMM- Ground Motion Model

Figure 1.1: Flowchart showing different steps of the ground motion selection based on NBCC 2020 (2022) adopted in the present study.

1.1 Problem Formulation

The following objectives are set for the present study:

- Implementation of the latest Canadian Seismic Hazard Model for site-specific hazard assessment. The site characteristics, such as the average shear-wave velocity in the uppermost 30 m (V_{s30}) are used as direct inputs.
- Assessment of uncertainties in the seismic hazard.
- Carry out disaggregation of the seismic hazard to ascertain the highest contributing sources and scenarios for a specific return period.
- Selection of hazard-consistent ground motion selection targeting site-specific seismic hazard. Prominent international strong-motion databases consisting of

shallow crustal and subduction zone earthquakes (Ancheta et al., 2014; NIED, 2019) are used for the selection.

- Parametric study on the effects of different inputs (such as targeted period range, conditioning period, and the return period of interest) to the ground motion selection.
- Effects of different parameters for the selection of site- and structure-specific ground motion on the nonlinear structural performance of a single-degree-of-freedom oscillator.

1.2 Organization of Report

Figure 1.1 shows the procedure adopted in the present report, organized as follows. Chapter 2 presents the implementation of the latest Canadian seismic hazard model (steps 1 to 3) and a background of the probabilistic seismic hazard analysis. Chapter 3 presents the hazard-consistent ground motion selection method (steps 4 to 6). Chapter 4 presents parametric studies for ground motion selection and shows different examples of ground motion suites with changes in periods, target spectrum, and scaling limits. Effects of ground motion suite on the nonlinear fragility assessment of a widely used hysteretic model is also presented.

Chapter 2

Seismic Hazard Model based on National Building Code of Canada 2020

A study of the large-scale motion of the Earth's outermost layer called the Lithosphere (extending 70–100 km from the surface), reveals the underlying cause behind the earthquakes as differences in mechanical properties of the layer beneath. The movement of the boundaries of adjacent plates makes the underground rock rupture suddenly. The extent (length, width, and location) of the rupture and shaking caused by this can be estimated with some confidence. However, the time and precise nature of the break and shaking remain unpredictable at present. The uncertainties in recorded shaking are reflected in the scale of observed recording on ground motion shaking parameters, such as peak ground acceleration (PGA). Even for a given event and distance from the epicenter, two stations can have intensity measure recordings, which are different by orders of magnitude. Thus, a probabilistic framework is adopted for seismic hazard assessment.

Assessment of PGA and spectral acceleration due to a given earthquake in the form of empirical equations is an important step for Seismic Hazard Analysis (SHA). This process is often based on statistical regression of collected data over a certain period in the areas subjected to similar kinds of plate movements. Such models are called Ground Motion Models (GMM).

There are primarily two kinds of SHA—Deterministic Seismic Hazard Analysis (DSHA)

and Probabilistic Seismic Hazard Analysis (PSHA). As the name suggests, DSHA assumes the occurrence of a characteristic earthquake at a source-to-site distance. PSHA, on the other hand, considers all sources capable of causing damage, with a range of possible magnitudes (due to the varying magnitude and source-to-site distance) caused by them. Since sufficient data pointing to something else (often by the use of DSHA) are rarely available, PSHA offers a framework where the multitude of uncertainties can be identified, quantified, and combined rationally to represent a complete picture of the seismic hazard (Baker et al., 2021).

Seismic events are highly probabilistic in that even the same magnitude-distance pair can produce widely varying effects on a given structure. In addition, the structural behavior of buildings is complex depending on the distribution of random variables, such as material strength, hysteretic properties, and section geometry. To understand the seismic performance of buildings, earthquake engineering is best studied through a probabilistic framework. First-generation seismic assessment guidelines (ATC 40, 1996; FEMA 273, 1997; FEMA 356, 2000) were limited in their capability of predicting seismic responses probabilistically.

Natural Resources Canada (NRCan) is entrusted with mapping active faults and developing reliable seismicity models in Canada. With approximately 10 million square km of area, studying Canada's seismicity is challenging. Over the last sixty years, incrementally detailed seismic hazard models for Canada have been developed. As a general trend, these advancements have resulted in increased seismic hazard estimates. The Canadian seismic hazard in the National Building Code of Canada, NBCC (2022) has undergone a comprehensive change. The 6th generation seismic hazard model (SHM6) developed by NRCan for the NBCC 2022 update considers newly-discovered potentially active faults, new GMMs, and precise source modeling for the great subduction and deep in-slab earthquakes (Kolaj et al., 2020a). Figure 2.1 shows the trend of change in the seismic hazard for selected locations in Canada, from East to West. A large increase (in the range of 20% to 100%) is observed in all regions across Canada. This has a lasting impact on the design and prevalent performance assessments of Canadian buildings.

In the present chapter, the latest open-source seismic hazard model has been used to characterize the hazard of locations across Canada. A methodology for assessment of the seismic hazard curve and disaggregation results (dominant earthquake

characteristics on the site of interest) based on SHM6 (Kolaj et al., 2020b) is discussed along with illustrations. Further, uncertainties in hazard are discussed, and its quantification using the model is explained with examples. Finally, the chapter shows examples of ground motion selection matching a site's characteristics and structure. To that end, two approaches for ground motion selection are explored—(1) Conditional Spectrum (CS) (Baker, 2011) and (2) generalized conditional intensity measure (GCIM) (Bradley, 2010). Two extensive global strong-motion databases for the ground motion selection are considered in the present study–(1) NGA-west of USA (Ancheta et al., 2014) and KiK-net of Japan (Okada et al., 2004).

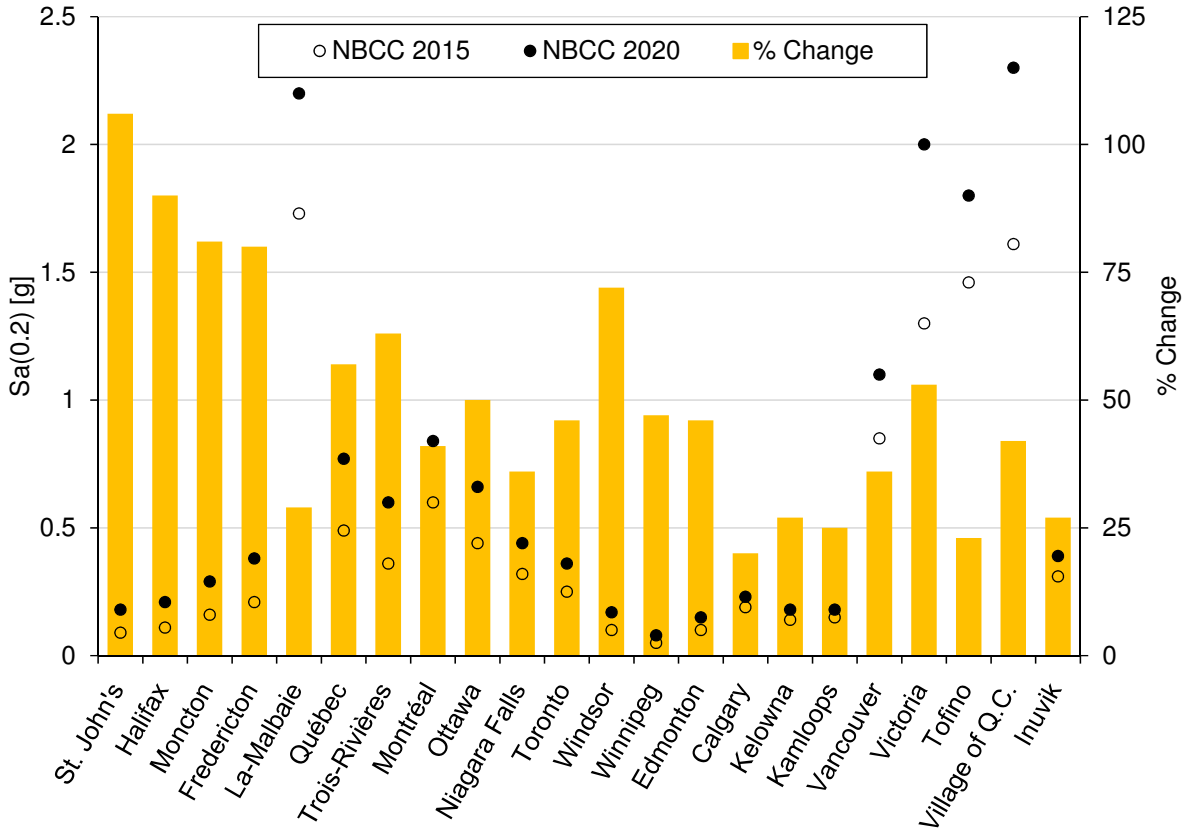

Figure 2.1: Change in seismic hazard from NBCC (2015) to NBCC 2020 (2022) for selected locations in Canada, from east to west. Intensity measure- $Sa(0.2)$; Return Period- 2475 year; Site Class- C.

2.1 Seismic Hazard Models of Canada

NRCan has adopted the latest SHM6 for Canada for seismic hazard maps of NBCC 2020 (2022). The latest maps are an improvement over the 5th generation SHM of NBCC (2015) as follows (Adams et al., 2019):

- Updated activity rate of the Cascadia megathrust earthquakes due to the addition of four complete rupture earthquakes to the hazard model for NBCC (2015).

- Updating earthquake sources for the deep inslab earthquakes under the Strait of Georgia. Improved modeling of the dip of the inslab source and the spatial activity rate.

- Addition of the Leech River Valley - Devil Mountain's faults near Victoria, BC (Halchuk et al., 2019). Goda and Sharipov (2021) independently assessed the effect of this addition on hazard and risk values in Victoria and found it to be in the range of 10–30% for high return periods.

- Use of modern GMMs (Kolaj et al., 2020a).

- Direct consideration of site class using V_{s30} in the hazard calculation compared to the earlier method of calculating for reference class C and then modifying it for different site classes.

- Use of open-source tool `OpenQuake` (GEM, 2022) for the hazard calculation.

Figure 2.2 shows the historical seismicity of Canada. The figure also shows the regionalization of Canada into East and West due to different wave propagation characteristics in the crust.

Four steps of PSHA are summarized below.

1. *Source identification*- Contrary to considering the fixed distance between the site and the source in DSHA, PSHA identifies all potential seismic sources in the study region. Next, each source is characterized by a distribution of its rupture location. In the absence of sufficient information, a uniform rupture probability is assumed for the entirety of fault geometry. The probability distribution of source-to-site distance is then obtained by combining rupture location, source geometry, and site location. Due to a large number of calculations, seismic sources are discretized, and the source-to-site distance is calculated for the discretized sources.

2. *Recurrence relationship*- The probability distribution of earthquake magnitude for each source is given by a recurrence relationship. The Gutenberg-Richter

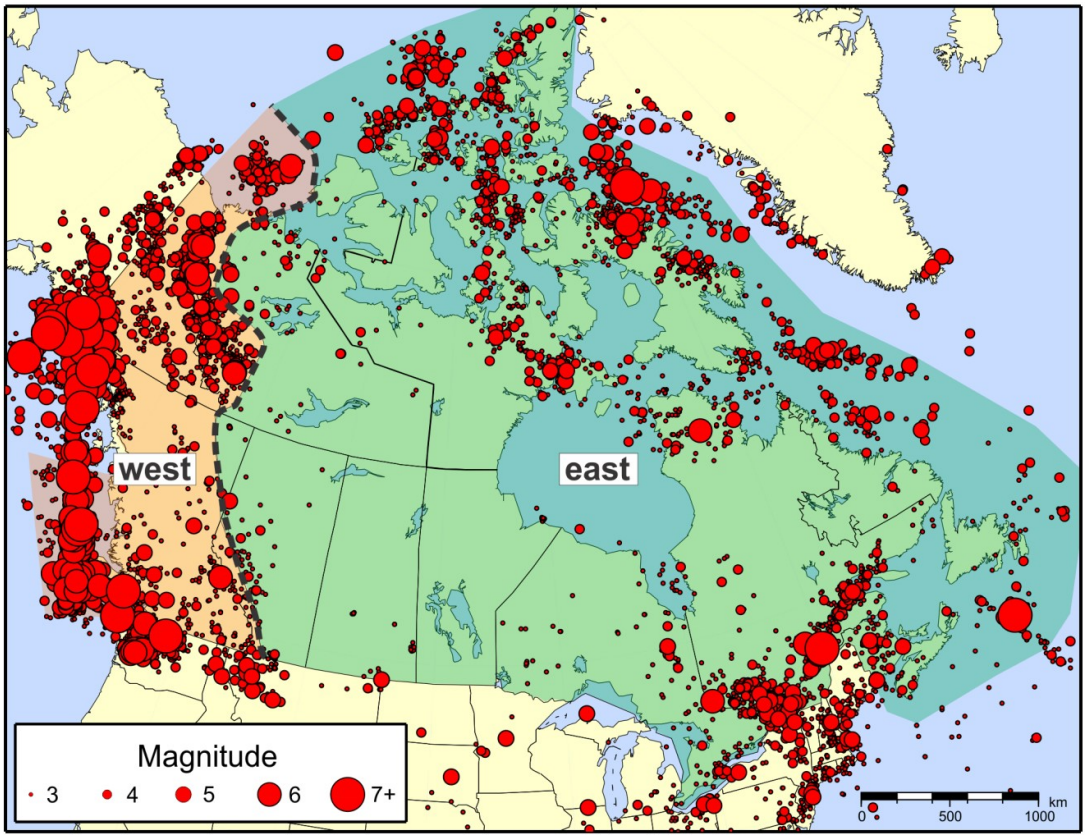

Figure 2.2: Earthquakes in Canada. The division of regions into Eastern and Western Canada for 6th generation SHM in NBCC (2022) are shown using dashed gray line (Adams et al., 2019).

(GR) law is typically used to relate the number of earthquakes in a region:

$$\log_{10}(\lambda_m) = a - bm, \tag{2.1}$$

where λ_m is the rate of earthquakes with a magnitude greater than m. Coefficients a and b are calculated from the statistical analysis of historic seismicity data for the region (Gutenberg and Richter, 1944). The unbounded form of the GR law in (2.1) assigns non-zero probabilities to large magnitudes of earthquakes, which may not be physically possible. Similarly, earthquakes smaller than a certain magnitude may not be of engineering importance. Thus, the GR law is modified as follows:

$$F_M(m) = \frac{1 - 10^{-b(m-m_{\text{min}})}}{1 - 10^{-b(m_{\text{max}}-m_{\text{min}})}}, \tag{2.2}$$

where $F_M(m)$ is the cumulative distribution function (CDF), m_{max} is the maximum possible magnitude (based on the historical and geological data), and m_{min} is the minimum earthquake magnitude of interest (based on the

engineering importance). Similar to source-to-site distance, the distribution of the earthquake magnitude is discretized for hazard assessment.

3. *Ground motion model*- For a given pair of magnitude and distance for a specific source (or source zone), the ground motion intensity can be predicted using GMM, which are obtained using recorded intensities for past earthquakes in the region under study or in the absence of sufficient data, similar seismic source. The GMM quantifies the inherent uncertainty in the estimated intensity. The mean and standard deviation of the log of intensity are often expressed by GMMs along with various other parameters. Several modern GMMs use the site's detailed seismological and geotechnical features to predict the intensity. An example of the modern GMM is Campbell and Bozorgnia (2008). The mean-log ground motion intensity is given by:

$$\ln \hat{Y} = f_{mag} + f_{dis} + f_{flt} + f_{hng} + f_{site} + f_{sed}, \tag{2.3}$$

magnitude term, $f_{mag} = \begin{cases} c_0 + c_1 M \text{ for } M \leq 5.5 \\ c_0 + c_1 M + c_2(M - 5.5) \text{ for } 5.5 < M \leq 6.5 \\ c_0 + c_1 M + c_2(M - 5.5) + c_3(M - 6.5) \text{ for } M > 6.5, \end{cases}$

distance term, $f_{dis} = (c_4 + c_5 M) \times \ln\left(\sqrt{{R_{RUP}}^2 + {c_6}^2}\right)$,

style of faulting term, $f_{flt} = c_7 \, F_{RV} f_{flt,Z} M + c_7 \, F_{NM}$,

hanging wall term, $f_{hng} = c_9 \, f_{hng,R} f_{hng,M} f_{flt,Z} f_{hng,\delta}$,

shallow site response term,

$f_{site} = \begin{cases} c_{10} \, \ln\left(\frac{V_{s30}}{k_1}\right) + k_2 \left\{\ln[A_{1100} + c\left(\frac{V_{s30}}{k_1}\right)^n] - \ln[A_{1100} + c]\right\} \text{ for } V_{s30} \leq k_1 \\ (c_{10} + k_2 n) \, \ln\left(\frac{V_{s30}}{k_1}\right) \text{ for } k_1 \leq V_{s30} \leq 1100 \\ (c_{10} + k_2 n) \, \ln\left(\frac{1100}{k_1}\right) \text{ for } V_{s30} > 1100, \end{cases}$

and basin response term, $f_{sed} = \begin{cases} c_{11}(Z_{2.5} - 1) \text{ for } Z_{2.5} < 1 \\ 0 \text{ for } 1 \leq Z_{2.5} \leq 3 \\ c_{12} k_3 e^{-0.75} \left[1 - e^{-0.25(Z_{2.5} - 3)}\right] \text{ for } Z_{2.5} > 3. \end{cases}$

The error in the intensity estimation is given in a table corresponding to different intensity measures. Thus, the GMMs depend on both source and site conditions.

The source parameters include rupture length, rupture width, rupture area (Wells and Coppersmith, 1994), magnitude, dip angle, slip pattern, and the site-specific parameters include shear wave velocity (V_{s30}) and soil type. Some of the next-generation GMMs developed as part of NGA-West (Power et al., 2008) are AS08 (Abrahamson and Silva, 2008), BA08 (Boore and Atkinson, 2008), CB08 (Campbell and Bozorgnia, 2008), and CY08 (Chiou and Youngs, 2008). With new data and tools, these GMMs have been updated as part of NGA-West2 (Bozorgnia et al., 2014). The updated GMMs are ASK14 (Abrahamson et al., 2014), BSSA14 (Boore et al., 2014), CB14 (Campbell and Bozorgnia, 2014), and CY14 (Chiou and Youngs, 2014), respectively. For SHM6 of NBCC (2022), these four GMMs are used for Active Crust tectonic regimes with equal weight. On the other hand, for the Subduction Inslab regime, Aea15 (Abrahamson et al., 2016), Zea06 (Zhao et al., 2006), AB03 (Atkinson and Boore, 2003), and Gea05 (García et al., 2005) are used with equal weight. For the Subduction Interface regime, the used GMMs are Aea15 (Abrahamson et al., 2016), Zea06 (Zhao et al., 2006), GA14 (Ghofrani and Atkinson, 2014), and AM09 (Atkinson and Macias, 2009).

4. *Combination of the uncertainties*- Probabilistic distributions of magnitude, distance, and resulting intensities are combined using the total probability theorem. This gives the probability of exceedance of specific intensity measure values.

$$\lambda(IM > x) = \sum_{i=1}^{n_{sources}} \lambda_i(m_{min}) \sum_{j=1}^{n_M} \sum_{k=1}^{n_R} \mathrm{P}(IM > x \,|\, m_j, r_k)\mathrm{P}(M_i = m_j)\mathrm{P}(R_i = r_k), \tag{2.4}$$

where $n_{sources}$ is the number of seismic sources; n_M and n_R are the number bins for magnitude and distance, respectively; λ_i is the activity rate for i-th source; the probability $\mathrm{P}(IM > x \,|\, m_j, r_k)$ is given by GMMs (Step 3); PDFs for distance and magnitude of i-th source are discretized to calculate $\mathrm{P}(M_i = m_j)$ and $\mathrm{P}(R_i = r_k)$, respectively (Step 1 and Step 2).

It is worth noting that while the above method is based on numerical integration, the PSHA calculations can be alternatively performed using stochastic event sets. This approach estimates the likelihood of earthquake-induced ground motion by simulating many potential earthquakes and calculating the resulting ground motion. `OpenQuake` (2022) uses stochastic event-based modeling approach.

2.1.1 Classification of Uncertainties

Probabilistic calculations involved in PSHA capture the large uncertainty associated with the effects of earthquakes. Two broader classifications of uncertainties are *aleatory* and *epistemic*. There are key differences in the way they are treated. The inherent variability in the process (e.g., fault rupture) constitutes the aleatory variability. These variations represent the uncertainties in the event itself. On the other hand, epistemic uncertainties arise from the lack of sufficient data or understanding (or mathematical representations thereof) of the process. These uncertainties can be reduced with newer earthquake recordings, if available, or advancement in the research. Examples of epistemic uncertainties are those in the recurrence relation and the values of maximum earthquake magnitude, $m_{\max}$.

2.1.2 Logic Tree

Logic trees are used for characterizing epistemic uncertainty in PSHA. Figure 2.3 shows An example logic tree. In this simplified example, two GMMs were considered applicable for the region – Campbell-Bozorgnia (CB) and Abrahamson-Silva (AS). The weights represent the level of relative applicability of different branches, e.g., 0.6 for CB and 0.4 for AS. Similarly, magnitude distribution and maximum magnitude are considered to follow two branches. Each branch is associated with different weights, which sum up to 1. Subsequently, calculations for each branch are carried out independently and then the final hazard estimates are obtained by taking the weighted average of each branch. The assignment of suitable weights to the logic tree branches is critically studied in the literature (Bommer et al., 2005; Bommer and Scherbaum, 2008; Scherbaum and Kuehn, 2011; Runge and Scherbaum, 2012).

2.1.3 Uniform Hazard Spectrum

A site-specific seismic hazard curve for an intensity measure (e.g., PGA) is obtained by plotting different values of the particular intensity measure against their probabilities of exceedance as given by (2.4). Hazard curves corresponding to different spectral accelerations are combined by fixing a probability of exceedance (or return period) in order to obtain a uniform hazard spectrum.

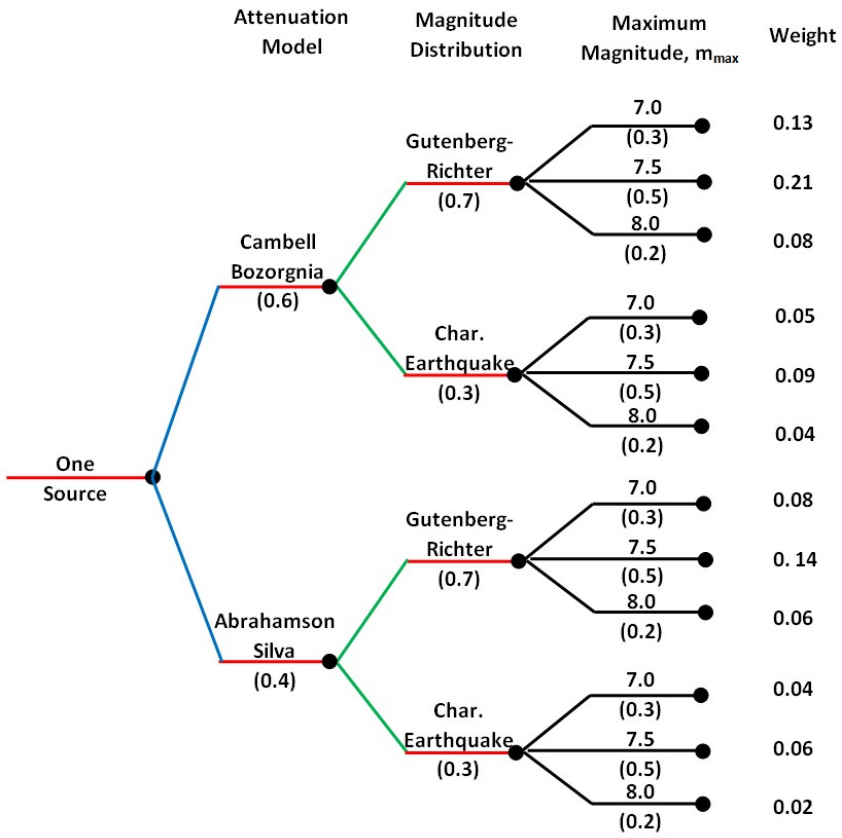

Figure 2.3: An example logic tree (based on Kramer, 1996)

2.1.4 Disaggregation

A single or a few representative earthquakes for a specific site corresponding to a return period are often required for planning purposes (e.g., scenario studies) or analytical assessment (e.g., spectral shape factor for ground motion selection, discussed later in Section 3.2.1 in detail). Since PSHA includes all possible earthquake sources and rupture-to-site distance combinations, the resulting hazard curve accumulates contributions from all possibilities in one curve. the reverse process of ascertaining a characteristic earthquake for a site condition on the return period (exceedance probability) is called *disaggregation*. Using Bayes' theorem, we have (Bazzurro and Cornell, 1999; McGuire, 1995):

$$\mathrm{P}(M = m_j, R = r_k \,|\, IM > x) = \frac{\lambda(IM > x \,|\, M = m_j, R = r_k)}{\lambda(IM > x)}, \tag{2.5}$$

where $\lambda(IM > x)$ is given by (2.4) and $\lambda(IM > x \,|\, M = m_j, R = r_k)$ is defined as follows:

$$\lambda(IM > x \mid M = m_j, R = r_k) = \sum_{i=1}^{n_{sources}} \big[\lambda(M_i > m_{\min})\mathrm{P}(IM > x \mid M = m_j, R = r_k) \\ \mathrm{P}(M_i = m_j)\mathrm{P}(R_i = r_k)\big] \quad (2.6)$$

Different magnitude-distance pairs are plotted in a three-dimensional plot to ascertain their contribution to the hazard. The magnitude-distance pair with the highest contribution is used as the characteristic earthquake for the site and return period of interest.

2.2 Implementation of Canadian Seismic Hazard Model

In the present section, the execution of PSHA calculation steps for site-specific hazard curves and disaggregation results are discussed. Procedures are explained through an example site of Vancouver City Center, British Columbia.

2.2.1 Seismic Hazard Curve

The sample job for obtaining seismic hazard curves is as follows:

```
[general]

description = Hazard Curves at Vancouver (SWCan 2020 NBCC
   Hazard-450 mps COLLAPSED RATES, 10 km area src disc)
calculation_mode = classical
random_seed = 23

[geometry]

sites = -123.12 49.25

[logic_tree]
```

```
number_of_logic_tree_samples = 0

[erf]

rupture_mesh_spacing = 5.0
width_of_mfd_bin = 0.1
area_source_discretization = 10.0

[site_params]

reference_vs30_type = measured
reference_vs30_value = 450.0
reference_depth_to_2pt5km_per_sec = 5.0
reference_depth_to_1pt0km_per_sec = 100.0

[calculation]

source_model_logic_tree_file =
   SW_CANADA_CIS_update_collapsed_source_model_logic_tree.xml
gsim_logic_tree_file = ..\..\shared\hdf_NBCC2020-
   W_reducedE_450mps_logic_tree.xml
intensity_measure_types_and_levels = {
              "PGA":  logscale(0.01, 4.0, 20),
              "SA(0.1)":  logscale(0.01, 4.0, 20),
              "SA(0.2)":  logscale(0.01, 4.0, 20),
              "SA(0.3)":  logscale(0.01, 4.0, 20),
              "SA(0.5)":  logscale(0.01, 4.0, 20),
              "SA(1.0)":  logscale(0.01, 4.0, 20),
              "SA(1.68)":  logscale(0.01, 4.0, 20),
              "SA(2.0)":  logscale(0.01, 4.0, 20),
              "SA(5.0)":  logscale(0.01, 4.0, 20)}

truncation_level = 5
investigation_time = 50.0
```

```
maximum_distance = {"Active Shallow Crust": 400.0, "Stable
   Shallow Crust": 600.0, "Subduction IntraSlab30": 400, "
   Subduction IntraSlab55": 400, "Subduction Interface":
   1000.0} # from AU model

[output]

export_dir = ./results
mean_hazard_curves = true
quantile_hazard_curves = 0.01 0.05 0.10 0.16 0.50 0.84 0.90
   0.95 0.99
hazard_maps = false
uniform_hazard_spectra = true
poes = 0.02 0.1 0.20
```

■

Both `rupture_mesh_spacing` and `area_source_discretization` are in km. For area sources, the area region is converted into point sources using the discretization size. and When analyzing multiple sites, a comma-separated value (`csv`) file can be used to input the longitude and latitude of all sites using the following command:

```
sites_csv = ..\..\shared\sampleSiteCoordinates.csv
```

The `.csv` file named `sampleSiteCoordinates.csv` is saved in the sub-directory named `shared`, which in turn is saved under the main repository. An example hazard curve obtained from the execution of the above example program is shown in Figure 2.4.

2.2.2 Uncertainty in Hazard Curve

The job file (`.ini`) discussed above (Section 2.2.1) for the hazard assessment can be tweaked to obtain different percentiles of the hazard assessment. In particular, the following line is used to obtain the 16%ile and 84%ile hazard curves in addition to the median hazard curve (represented by 0.50 quantile).

```
quantile_hazard_curves = 0.16 0.50 0.84
```

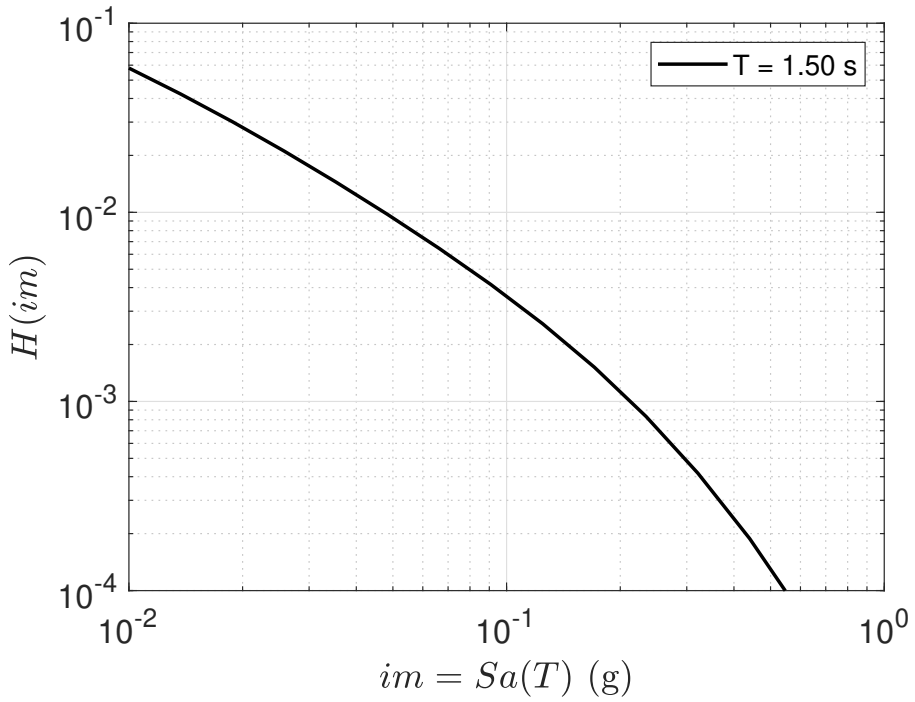

Figure 2.4: Hazard curve for Vancouver, BC for intensity measure $Sa(1.5)$ at a site with V_{s30} = 450 m/s.

Figure 2.5 shows the hazard curve shown in the previous section with $\pm 1\sigma$ uncertainty.

2.2.3 Uniform Hazard Spectrum

Using the procedure described in the previous section, a series of hazard curves for a given location can be obtained. The changes in the job file discussed in Section 2.2.1 can be incorporated as follows:

```
intensity_measure_types_and_levels = {"PGA": logscale
    (0.01,4.0, 20),
        "SA(0.1)": logscale(0.01,4.0, 20),
        "SA(0.2)": logscale(0.01,4.0, 20),
        "SA(0.5)": logscale(0.01,4.0, 20),
        "SA(1.0)": logscale(0.01,4.0, 20),
        "SA(2.0)": logscale(0.01,4.0, 20),
        "SA(4.0)": logscale(0.01,4.0, 20),
        "SA(5.0)": logscale(0.01,4.0, 20)}
```

Figure 2.6 shows the result of

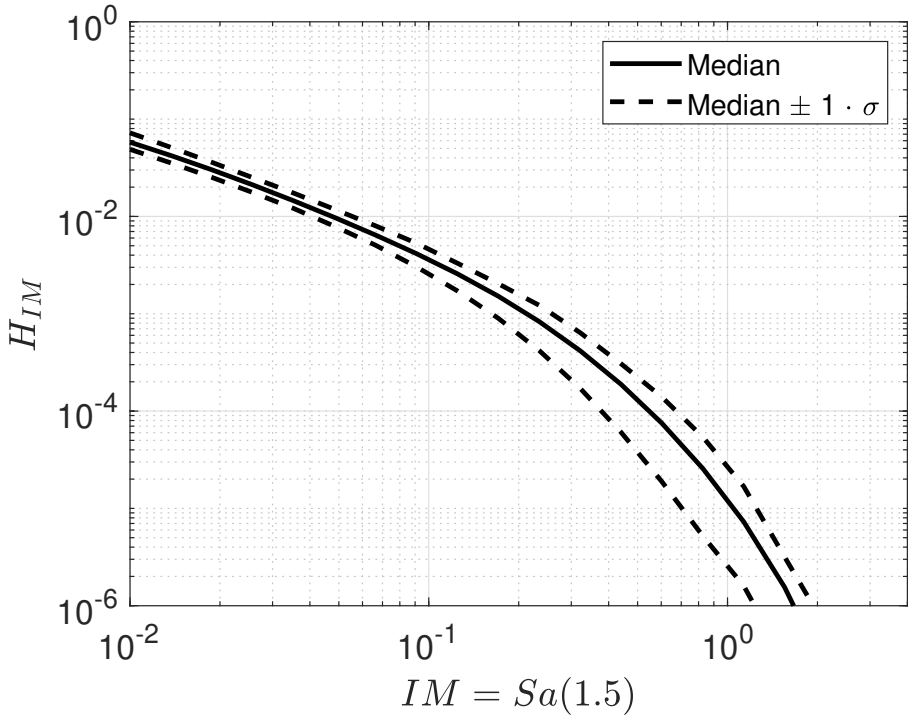

Figure 2.5: Median hazard curve along with $1 \pm \sigma$ for Vancouver, BC for intensity measure $Sa(1.5)$ at a site with V_{s30} = 450 m/s.

the intensity measures of $PGA, Sa(0.1\text{ s}), Sa(0.2\text{ s}), Sa(0.5\text{ s}), Sa(1\text{ s}), Sa(2\text{ s}), Sa(4\text{ s}),$ and $Sa(5\text{ s})$ for the example site of Vancouver City Center, BC.

Using a series of hazard curves for a particular location, a uniform hazard spectrum is developed by taking a slice for a fixed value of the probability of exceedance, H_{IM}. For example, Figure 2.7 shows uniform hazard spectra for 2%, 5%, and 10% probability of exceedance in 50 years (i.e., 2475, 975, and 475 years of the return period, respectively). These spectra can also be generated by directly changing the job file discussed in Section 2.2.1 under the `output` section of the program as follows:

```
uniform_hazard_spectra = true
poes = 0.02 0.05 0.1
```

It is worth noting that the program considers the probability of exceedance in 50 years, and the inputs are given in terms of the fraction.

2.3 Disaggregation

PSHA includes all possible earthquake sources around the site. Thus, the hazard curve for a location is an accumulation of contributions from all combinations of

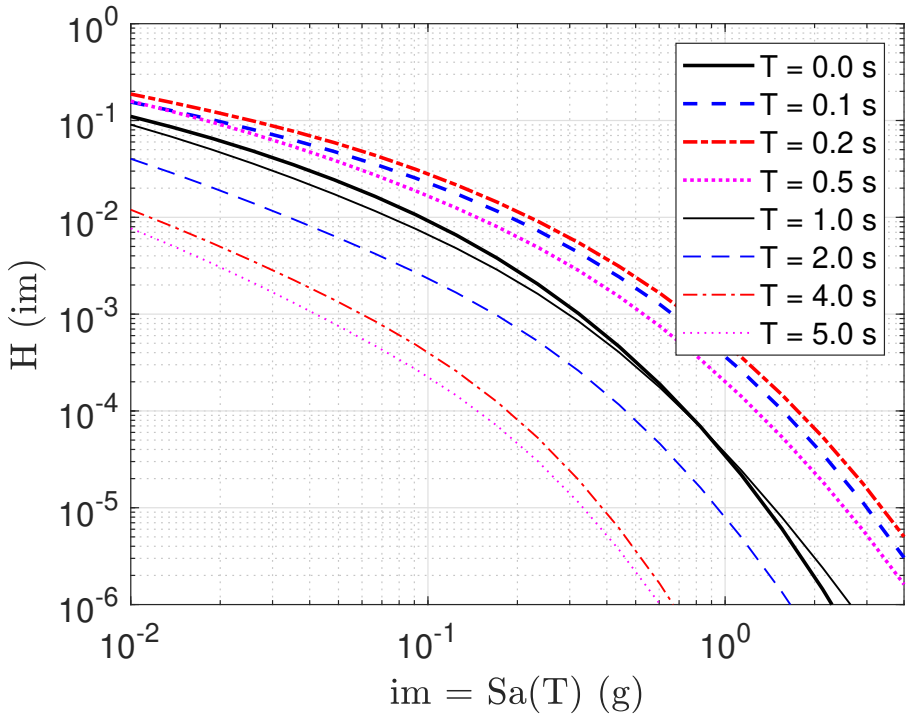

Figure 2.6: A series of hazard curves for Vancouver, BC corresponding to $Sa(T)$ for periods ranging from 0 to 5 s (V_{s30} = 450 m/s).

source, magnitude, and distance. It is of interest to structural engineers to ascertain the relative values of these different contributions for a specified value of spectral acceleration. This distribution of earthquakes, conditional on the event of spectral acceleration exceeding a value, is obtained using disaggregation. A general formulation for disaggregation was discussed in Section 2.1.4. A sample job in `OpenQuake` for obtaining disaggregation of hazard is as follows:

```
[general]

description = Disaggregation at Vancouver for Sa(1.5). 2475
   and 475 year of return period (SWCan 2020 NBCC Hazard-450
   mps COLLAPSED RATES, 10 km area src disc)
calculation_mode = disaggregation
random_seed = 23

[geometry]

sites = -123.12 49.25
```

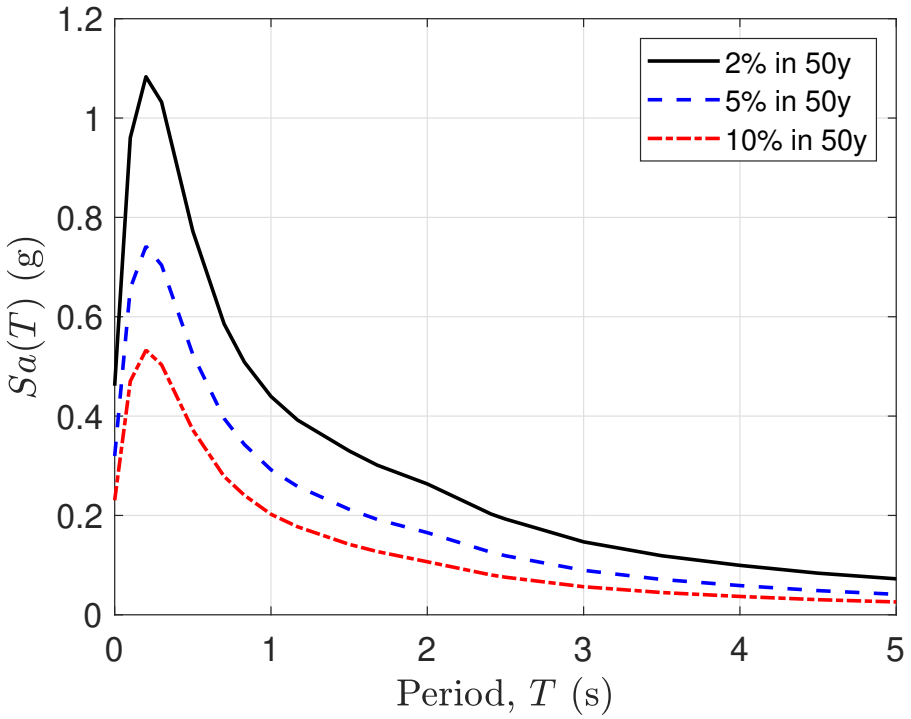

Figure 2.7: Uniform hazard spectrum for Vancouver, BC at a site with V_{s30} = 450 m/s based on seismic hazard model of NBCC 2020 (2022).

```
[logic_tree]

number_of_logic_tree_samples = 0

[erf]

rupture_mesh_spacing = 5.0
width_of_mfd_bin = 0.1
area_source_discretization = 10.0

[site_params]

reference_vs30_type = measured
reference_vs30_value = 450.0
reference_depth_to_2pt5km_per_sec = 5.0
reference_depth_to_1pt0km_per_sec = 100.0

[calculation]
```

```
source_model_logic_tree_file =
   SW_CANADA_CIS_update_collapsed_source_model_logic_tree.xml
gsim_logic_tree_file = ..\..\shared\hdf_NBCC2020-
   W_reducedE_450mps_logic_tree.xml
intensity_measure_types_and_levels =
                        {"SA(1.5)":  logscale(0.01, 4.0, 40)}
truncation_level = 3
investigation_time = 50.0
maximum_distance = 400.0
# maximum_distance = {"Active Shallow Crust": 400.0, "Stable
   Shallow Crust": 600.0, "Subduction IntraSlab30": 400, "
   Subduction IntraSlab55": 400, "Subduction Interface":
   1000.0} # from AU model

[disaggregation]

poes_disagg = 0.02 0.10
mag_bin_width = 0.10
distance_bin_width = 20.0
coordinate_bin_width = 2.0
num_epsilon_bins = 7

[output]

export_dir = ./results
```

■

`OpenQuake` determines the bins for ε on both sides of the median cumulative distribution for GMMs using the parameters `truncation_level` and `num_epsilon_bins`. Different return periods for disaggregation are assigned using the following code under the `disaggregation` section of `.ini` file:

```
poes_disagg = 0.02 0.1 0.2
```

Bin widths for magnitude and distance can be specified as follows:

Table 2.1: Disaggregation for earthquake types for Vancouver, BC at a site with V_{s30} = 450 m/s. $Sa(T)$ with period, T in seconds.

Intensity	T_r = 2475 years			T_r = 475 years		
Measure	Crustal	Interface	Intraslab	Crustal	Interface	Intraslab
PGA	15%	16%	**69%**	15%	17%	**68%**
$SA(0.2)$	16%	10%	**74%**	16%	13%	**72%**
$SA(1.0)$	**40%**	30%	30%	31%	29%	**40%**
$SA(1.5)$	**43%**	35%	22%	**35%**	32%	33%
$SA(2.0)$	**43%**	38%	19%	**34%**	**34%**	31%
$SA(3.0)$	**44%**	39%	17%	35%	**36%**	29%
$SA(5.0)$	38%	**48%**	13%	31%	**42%**	26%

```
mag_bin_width = 0.10
distance_bin_width = 20.0
```

Figure 2.8 shows the disaggregation results on the example site of Vancouver City Center for 2475 and 475 years of the return period. To understand the relative contributions of different types of tectonics, the following line under the `output` section of the job file saves source-specific contributions to the hazard.

```
individual_rlzs = true
```

Table 2.2: Disaggregation for earthquake types for Victoria, BC at a site with V_{s30} = 450 m/s.

Intensity Measure	T_r = 2475 years			T_r = 475 years		
	Crustal	Interface	Intraslab	Crustal	Interface	Intraslab
PGA	26%	4%	**70%**	25%	9%	**66%**
$SA(0.2)$	24%	4%	**72%**	24%	7%	**69%**
$SA(1.0)$	**52%**	41%	7%	38%	**42%**	21%
$SA(1.5)$	41%	**57%**	2%	34%	**54%**	12%
$SA(2.0)$	32%	**68%**	1%	31%	**61%**	8%
$SA(3.0)$	21%	**78%**	0%	26%	**69%**	5%
$SA(5.0)$	9%	**91%**	0%	20%	**77%**	3%

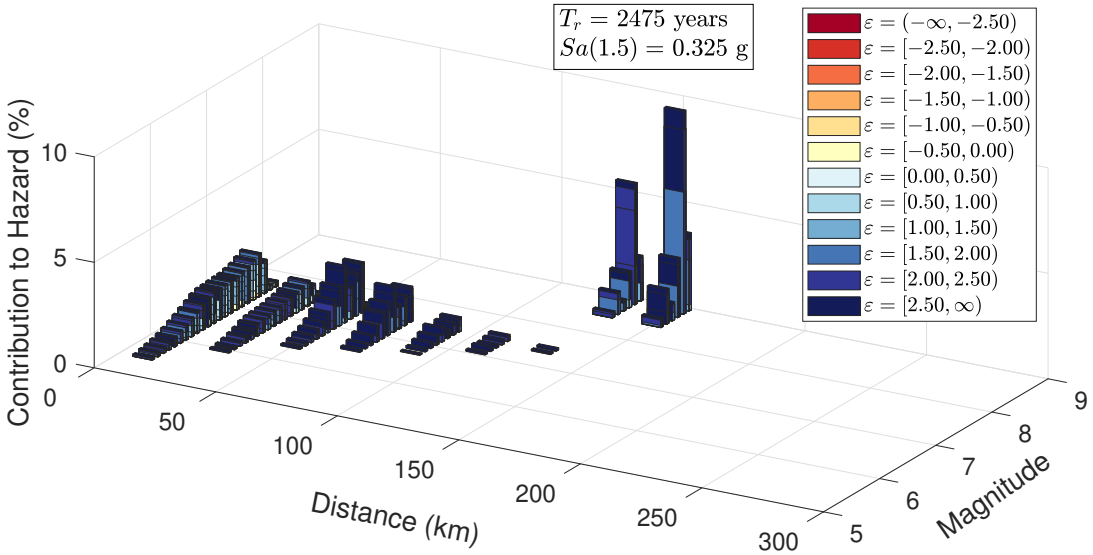

(a)

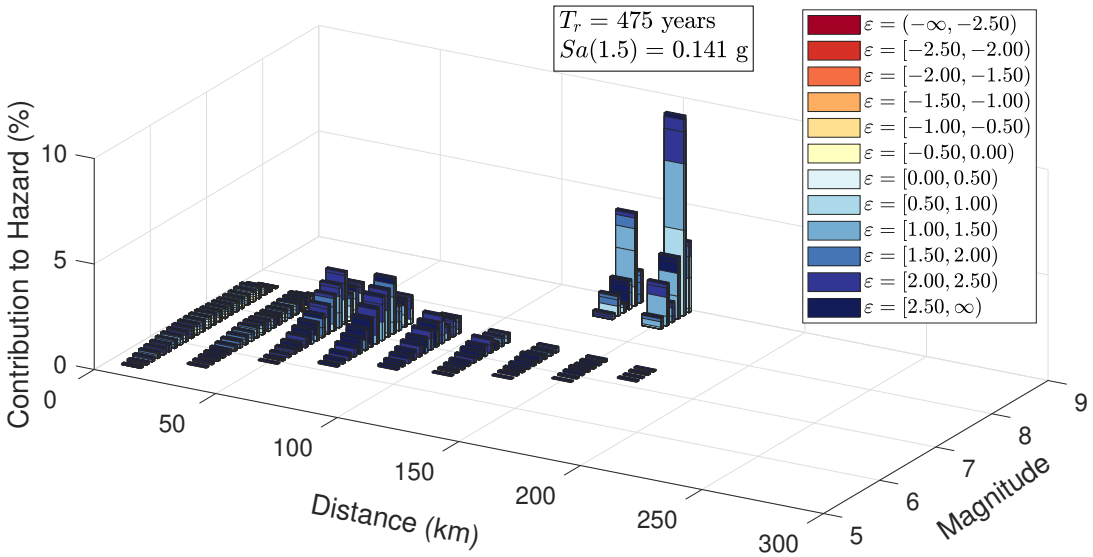

(b)

Figure 2.8: Disaggregation for Vancouver, BC for intensity measure $Sa(1.5)$ and return period of (a) 2475 years and (b) 475 years (bin sizes for disaggregation- $\Delta M = 0.1$, $\Delta R = 20$ km).

Chapter 3

Ground Motion Selection based on National Building Code of Canada 2020

As a general requirement, the seismotectonic environment and geotechnical conditions at the building location should be represented in the selected ground motion set. NBCC (2015) defines the methodology for selecting ground motion for rigorous non-linear analysis of buildings. The structural commentary to design standard recognizes that such special studies are primarily carried out in research environment (paragraph 179b of NRCC, 2015) and are expected to be rigorous in implementing the recommended approach. The structural commentary (NRCC, 2015) also lays out the guidelines for ground motion selection. The ground motion selection guidelines in the structural commentary are investigated in greater detail by Tremblay et al. (2015), which are in turn based on the corresponding guidelines set out by Haselton et al. (2014) for ASCE 7 (2016).

Figure 3.1 (reproduced from Chapter 1) shows the steps followed in the present study for the ground motion selection based on NBCC 2020 (2022). In the present chapter, steps 4 to 6 are described. Recommendations by structural commentary to NBC (NRCC, 2015) and a summary of conditional spectra are briefly discussed. Details of the ground motion selection are provided in subsequent sections.

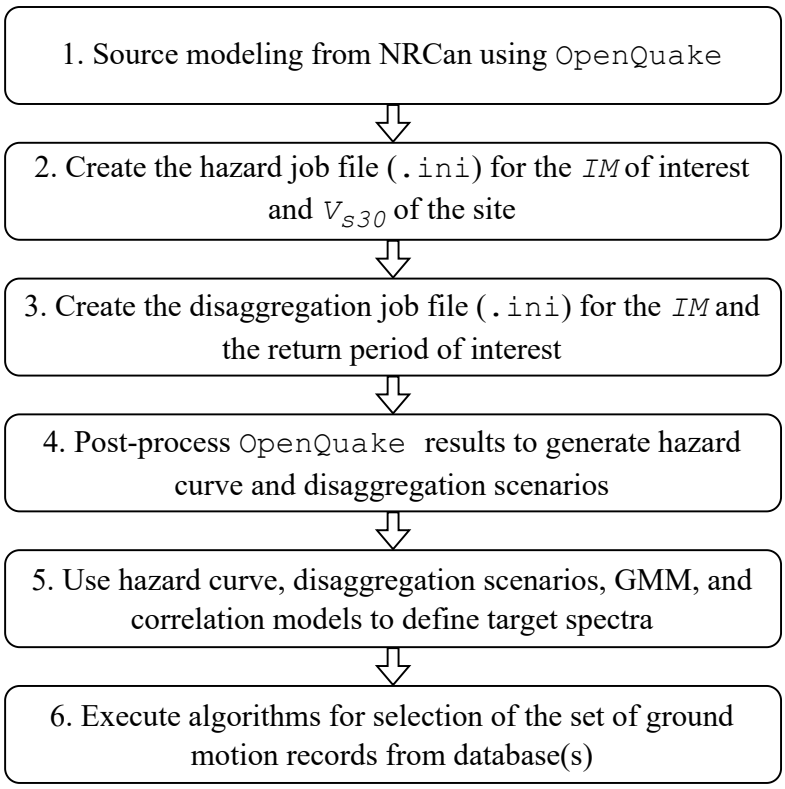

IM- Intensity Measure; V_{s30}- average shear-wave velocity in the uppermost 30 m (in m/s); GMM- Ground Motion Model

Figure 3.1: Flowchart showing different steps of the ground motion selection based on NBCC 2020 (2022) adopted in the present study.

3.1 Guidelines for Ground Motion Selection based on NBCC 2020

Based on the results of seismic hazard disaggregation, dominant magnitude-distance scenarios and sources (different tectonic environments) must be covered in the selected ground motion records. For example, Table 2.1 shows the contribution of different source zones for Vancouver, BC, as per the seismic hazard of NBCC 2020 (2022). The procedure for selecting ground motion suite and their target are summarized in the next few sections (NRCC, 2015).

3.1.1 Period Range of Interest

A suitable *period range of interest* $[T_{min}, T_{max}]$ must be covered in the selected ground motion records. This period range consists of the periods of vibration that contribute to the dynamic response of the building including the torsional modes, if any. The

upper bound of the period range, T_{max} is defined as $\max(2T_1, 1.5\,\text{s})$, where T_1 is the period of vibration in the first mode. The lower bound of the period range, T_{min} is defined as $\min(0.15T_1, T_{90\%})$, where $T_{90\%}$ is the lowest period of vibration that achieves a cumulative mass participation of 90%.

3.1.2 Target Response Spectrum

The target response spectrum (spectra) can be defined using one of the three methods depending on hazard disaggregation:

1. **Method A:** If a single response spectrum is targeted *based on the design spectrum*, the entire period range of interest can either be covered (a) by a single scenario earthquake (magnitude-distance combination), if one dominant earthquake exists or (b) by different period ranges for different dominating scenario combinations, if multiple tectonic sources contribute significantly to the location's seismicity. In the latter case, the scenarios can overlap each other and a minimum of one scenario-specific period range should be defined.
2. **Method B:** When the target spectrum is created by site-specific scenarios considering multiple earthquake-distance combinations and tectonic sources, the target can be obtained either by:
    - **Method B1:** creating spectra for *each dominant magnitude-distance combination and/or tectonic source* in the particular period range where it has significant contributions, or
    - **Method B2:** creating spectra for *each period of vibration modes* with significant contribution to building's dynamic response.

With the updated NBCC 2020 (2022), the need for site class factors is eliminated and the response spectra for continuous values of $V_{s,30}$ can be obtained either from the seismic hazard tool for NBCC 2020 (https://earthquakescanada.nrcan.gc.ca/hazard-alea/interpolat/nbc2020-cnb2020-en.php). Alternatively, the seismic hazard values can also be obtained by querying the NRCAN web-service in `json` format. The address for the GraphQL Application Programming Interface (API) is: https://www.earthquakescanada.nrcan.gc.ca/api/canshm/graphql.

In the present study, a rigorous and fundamental approach of performing probabilistic seismic hazard analysis from the source model using OpenQuake (GEM, 2022) is

adopted. This allows to obtain the seismic hazard curves for actual periods of interest and eliminates the need to interpolate standard hazard curves provided for PGA, $Sa(0.05)$, $Sa(0.1)$, $Sa(0.2)$, $Sa(0.3)$, $Sa(0.5)$, $Sa(1.0)$, $Sa(2.0)$, $Sa(5.0)$, and $Sa(10.0)$. In addition, the PSHA yields disaggregation results used later for the ground motion selection (under Method B).

3.1.3 Number of Ground Motion Records

The minimum number of records for Method A is 5 for each scenario-specific period range, with a minimum of 11 for all scenarios combined. For Method B, a suite of 11 or more records should be used for each source. The recommended number of records is intended for a median seismic demand of buildings and not the dispersion.

3.1.4 Scaling of Ground Motion

The scaling of ground motion is carried out in two stages. First, the ground motion records are individually scaled such that their response spectra match or exceed the target spectrum in the scenario-specific range of periods. The second stage scaling is applied on the entire suite such that the mean response spectrum of the suite is not less than the target spectrum by more than 10%. The limit on scaling is suggested to be between 0.5 and 4.

3.2 Hazard-Consistent Ground Selection Targeting Conditional Spectrum

Non-linear time-history analysis is considered to be the most rigorous numerical method to assess the seismic performance of buildings. Due to the large levels of uncertainty involved in earthquakes, a building is subjected to a series of time-history records. Generic ground motion sets have been proposed and widely adopted in the literature, for example, FEMA P695 (2009) lists a set of twenty-two pairs of recorded orthogonal time-history, called far-field records. FEMA P695 (2009) also defines a near-field ground motion set of twenty-eight pairs of ground motion records. These generic ground motion sets are proposed to be applicable regardless of the building characteristics and site hazard. However, the hazard spectra and seismic characteristics of one site varies from another depending on the seismotectonic

and geotechnical features. Thus, while generic ground motion sets are helpful in a benchmark assessment of a building's performance, it does not capture the characteristics of seismic hazard of the site and the building. The selection of site-specific ground motion set requires a target spectrum, a database of time-history records, and an algorithm to select a set of ground motion records that match the target spectrum. The issues of target spectrum and selection algorithms are discussed next. Details of the databases considered in the present study are discussed later in the chapter.

3.2.1 Conditional Mean Spectrum (CMS)

The UHS is used for the seismic design of buildings by design codes. Corresponding to a return period (e.g., 2% in 50 years), a UHS for a particular site can be estimated by using a series of hazard curves from the PSHA for different spectral acceleration and picking the points from each curve corresponding to the return period of interest. Each point on a UHS is independent of each other. In the force-based prescriptive design, only one point of the UHS is used at a time. Thus, the lack of correlation between spectral ordinates does not affect the design process. On the other hand, for the performance-based seismic design, nonlinear behavior of damaged buildings require simultaneous consideration of periods longer than the natural vibration mode. In addition, higher modes of vibration of a building are represented by shorter periods. Thus, the effects of correlation between spectral ordinates become crucial. The UHS-targeted ground motion selection is conservative due to the envelope of uncorrelated spectral ordinates with equal deviation from the mean. This is particularly applicable for (i) extreme events with higher spectral values and (ii) studies with objectives to estimate the collapse capacity.

Different models for correlation between spectral ordinates have been proposed in the literature (Inoue and Cornell, 1990; Baker and Jayaram, 2008; Baker, 2011). Figure 3.2 shows the values of correlation coefficient against the ratio of the vibration periods. The consistency in different proposed models shows their relative maturity despite availability of new data. A correlation coefficient of as high as 0.75 is observed for a period softening ratio of $\sim$2. This indicates a strongly correlated spectral ordinates even after a significant period softening.

The conditional mean spectrum (CMS) overcomes the limitations of UHS for the

selection of site-specific ground motion records (Baker, 2011). The spectral ordinates in a CMS is conditioned on the value of spectral acceleration at the conditioning period T^*. The fundamental period of vibration of the building is often used for T^*. The *spectral value* ε of a location is defined as the number of standard deviations that the seismic hazard ($Sa(T^*)$, as obtained from PSHA) is away from the median predicted spectral value for an earthquake, e.g., the disaggregated magnitude-distance pair, $(\overline{M}, \overline{R})$.

$$\varepsilon(T^*) = \frac{\ln Sa(T^*) - \mu_{\ln Sa(T^*)}}{\sigma_{\ln Sa(T^*)}}. \tag{3.1}$$

where $\mu_{\ln Sa(T^*)}$ and $\sigma_{\ln Sa(T^*)}$ are obtained from a suitable GMM for $(\overline{M}, \overline{R})$. Conditional on the value of $\varepsilon(T^*)$, CMS is mathematically expressed as

$$\ln[Sa(T_i)|Sa(T^*)] = \mu_{\ln Sa(T_i)} + \rho_{\varepsilon(T_i),\varepsilon(T^*)}\sigma_{\ln Sa(T_i)}\varepsilon(T^*), \tag{3.2}$$

where $\rho_{\varepsilon(T_i),\varepsilon(T^*)}$ is the correlation coefficient between spectral ordinate at T_i and T^*; $\mu_{\ln Sa(T_i)}$ and $\sigma_{\ln Sa(T_i)}$ are obtained from the GMM. In summary, while the UHS is defined by $Sa(T_i)$, the CMS is defined by $Sa(T_i)|Sa(T^*)$. Inoue and Cornell (1990) proposed a simple expression for correlation coefficient of spectral ordinates $\rho_{\varepsilon(T_i),\varepsilon(T^*)}$ as follows:

$$\rho_{\ln Sa(T_1),\ln Sa(T_2)} = 1 - 0.33|\ln(T_1) - \ln(T_2)|. \tag{3.3}$$

Using the updated database of NGA-West, an updated correlation model was proposed as follows (Baker and Jayaram, 2008):

$$\begin{aligned}
&\text{if } T_{\max} < 0.109,\ \rho_{\ln Sa(T_1),\ln Sa(T_2)} = C_2\\
&\text{else if } T_{\min} > 0.109,\ \rho_{\ln Sa(T_1),\ln Sa(T_2)} = C_1\\
&\text{else if } T_{\max} < 0.2,\ \rho_{\ln Sa(T_1),\ln Sa(T_2)} = \min(C_2, C_4)\\
&\text{else } \rho_{\ln Sa(T_1),\ln Sa(T_2)} = C_4,
\end{aligned}$$

where the coefficients are given by:

$$C_1 = 1 - cos\left(\frac{\pi}{2} - 0.366\ln\left(\frac{T_{\max}}{\max(T_{\min}, 0.109)}\right)\right)$$

$$C_2 = \begin{cases} 1 - 0.105\left(1 - \frac{1}{1+e^{100T_{\max}-5}}\right)\left(1 - \frac{T_{\max}-T_{\min}}{T_{\max}-0.0099}\right) & \text{if } T_{\max} < 0.2 \\ 0 & \text{otherwise} \end{cases}$$

$$C_3 = \begin{cases} C_2 & \text{if } T_{\max} < 0.109 \\ C_1 & \text{otherwise} \end{cases}$$

$$C_4 = C_1 + 0.5\left(\sqrt{C_3} - C_3\right)\left(1 + \cos\left(\frac{\pi T_{\min}}{0.109}\right)\right),$$

where $T_{\min}$ and $T_{\max}$ are the limits of the periods range. Figure 3.2 compares these correlation coefficient models.

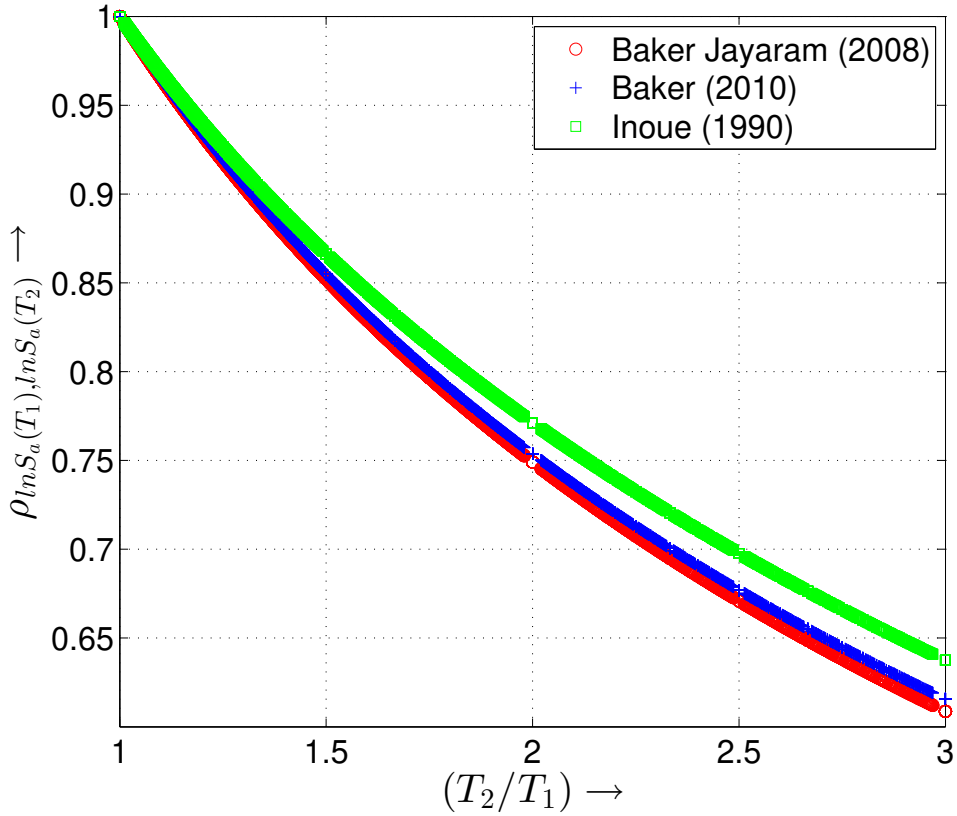

Figure 3.2: Comparison of different correlation coefficient expressions between spectral ordinates, $\rho_{\ln Sa(T_1),\ln Sa(T_2)}$.

Figure 3.3 shows an example CMS with the conditioning period, $T^* = 1.32$ s. Using GMM by Abrahamson and Silva (1997) and a characteristic earthquake of $\overline{M} = 7.30$ and $\overline{R} = 23.6$ km, ε was calculated as +1.26.

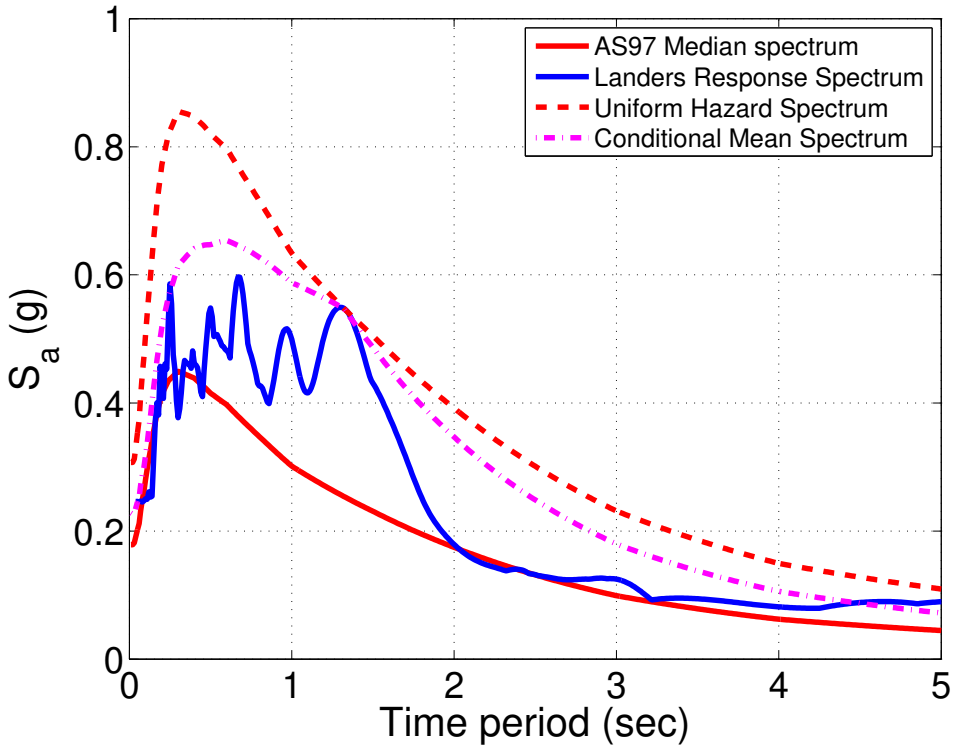

Figure 3.3: Generation of conditional mean spectrum for the Landers (1992) earthquake with conditioning period, $T^* = 1.32$ s. Abrahamson and Silva (1997) was used as GMM ($\overline{M} = 7.30$ and $\overline{R} = 23.6$ km)

3.2.2 Algorithm for Hazard-Consistent Ground Motion Selection

Targeting Conditional Mean Spectrum: For targeting a CMS, the error between target Sa_{CMS} and the records' response spectra is minimized. The time histories with the smallest total deviation are selected based on the sum of squared error SSE_k in the logarithmic values (Buratti et al., 2010).

$$SSE_k = \sum_i \left(\ln Sa_{CMS}(T_i) - \ln Sa_k(T_i)\right)^2, \tag{3.4}$$

where subscript k denotes the earthquake record index, and i is the period index that runs over the period range of interest. ASCE 7 (2010) recommends a range of $0.2T_1 - 1.5T_1$, where T_1 is the fundamental period of the structure. Recent research assessing the collapse suggests that period elongation of structures makes them sensitive to a longer range. Baker (2011) recommended considering the period range of $0.2T_1 - 2T_1$.

Targeting Conditional Spectrum (Conditional Mean Spectrum and its Covariance): While targeting CMS is appropriate for capturing the central tendency of the structural response, aleatory uncertainties in the ground shaking must be reflected in the selected ground motion set to estimate the dispersion in the structural response. An inappropriate consideration of the uncertainty in ground motion records can lead to an underestimation of the record-to-record variability of structural response and, in turn, to an underestimation of seismic risk. For an example ground motion selection at Vancouver City Hall, Figure 3.4a shows the selection of 20 ground motion records targeting CMS, whereas Figure 3.4b shows the selected ground motion set targeting both, the CMS and conditional covariance of spectral ordinates. For comparison purposes in this example, both ground motion suites are selected for Shallow Crustal earthquakes. The conditioning period was considered as $T^* = 1.17$ s. The disaggregated magnitude-distance for the Crustal earthquakes at the location is $\overline{M} = 7.35, \overline{R_{JB}} = 15$ km. Using CB14 (Campbell and Bozorgnia, 2014) as the GMM, the spectral value $\bar{\varepsilon} = 0.777$. All ground motion records were selected from the NGA-West2 database (Ancheta et al., 2014).

Conditional spectrum (CS) is the combination of CMS with the conditional covariance matrix. Jayaram and Baker (2008) showed that the logarithmic spectral acceleration at various periods follows a multivariate normal random distribution. Thus, the statistical parameters for CS can be obtained using the joint multivariate normal distributions. To select the ground motion records targeting a CS, Jayaram et al. (2011) proposed a matching algorithm. First, the target CMS is quantified using (i) the uniform hazard spectrum and disaggregated magnitude-distance tuple $(\overline{M}, \overline{R})$ from PSHA, and (ii) the spectral value $\varepsilon(T^*)$ for the example site for the conditioning period T^* and a suitable GMM. Next, the conditional covariance matrix for the CS is determined using $\varepsilon(T^*)$ for the location and the correlation model between spectral ordinates (e.g., Baker and Jayaram, 2008). The algorithm begins by generating random multivariate normal realizations of response spectra with the statistical parameters (mean vector and covariance matrix) of the target CS. Each realization of the response spectrum is then compared with the response spectrum of each ground motion record in the available database. For each realization, the response spectrum with minimum SSE_k, as defined in (3.4), is selected. Correspondingly, a set of time-history records from the database is obtained that represents the multivariate lognormal random distribution given by CS. The selected ground motion set is fine-

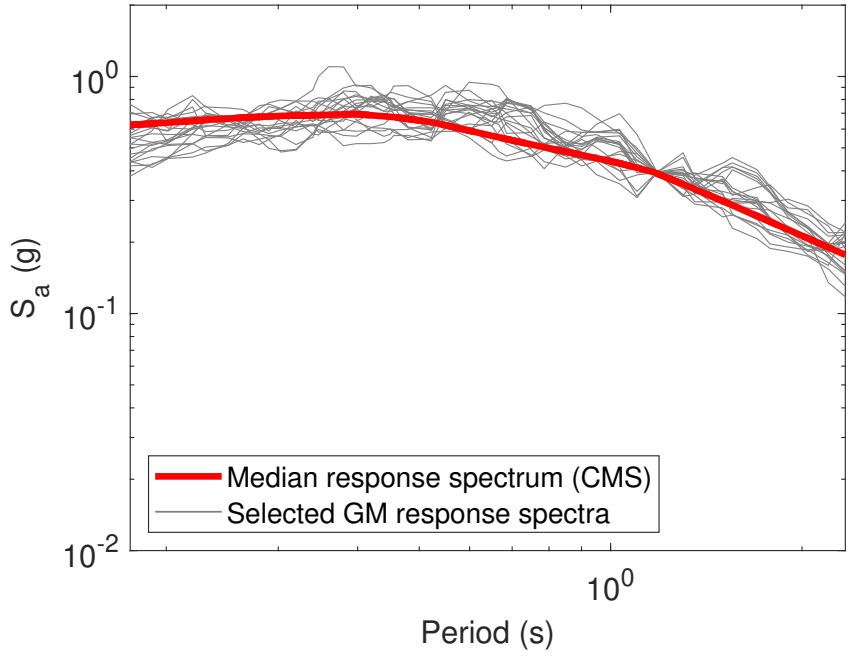

(a)

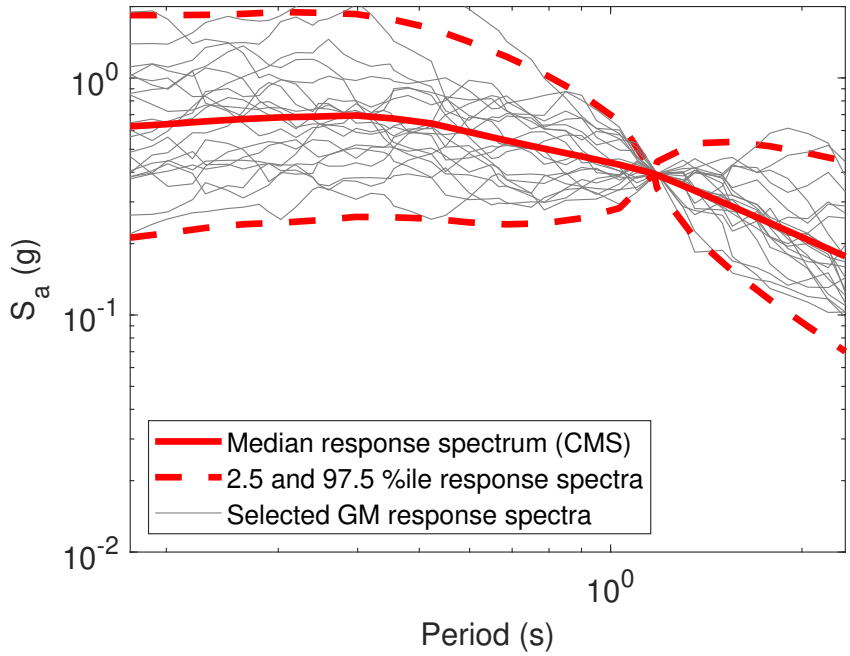

(b)

Figure 3.4: Selection of 20 ground motion records targeting (a) only CMS and (b) CMS with conditional covariance for an example site of Vancouver.

tuned by employing a greedy algorithm where each record is individually attempted to be replaced by one of the remaining unused records in the database so as to find a better match with the target covariance (Baker, 2011).

For multivariate normal random distribution of $\boldsymbol{X} = \begin{bmatrix} \boldsymbol{X_1} \\ \boldsymbol{X_2} \end{bmatrix}$ with mean $\boldsymbol{\mu} = \begin{bmatrix} \boldsymbol{\mu_1} \\ \boldsymbol{\mu_2} \end{bmatrix}$ and unconditional covariance as $\boldsymbol{\Sigma} = \begin{bmatrix} \boldsymbol{\Sigma_{11}} & \boldsymbol{\Sigma_{12}} \\ \boldsymbol{\Sigma_{21}} & \boldsymbol{\Sigma_{22}} \end{bmatrix}$, covariance of $\boldsymbol{X_1}$ conditional on $\boldsymbol{X_2} = \boldsymbol{x_2}$ is given by (Johnson et al., 2002):

$$\boldsymbol{\Sigma}_{\boldsymbol{X1}|\boldsymbol{X_2}=\boldsymbol{x_2}} = \boldsymbol{\Sigma_{11}} - \boldsymbol{\Sigma_{12}}\boldsymbol{\Sigma_{22}^{-1}}\boldsymbol{\Sigma_{21}}. \tag{3.5}$$

Following are the steps to find a CS-targeted ground motion set having N_0 number of time-history records:

Step 1: Using disaggregation of PSHA, find the characteristic tuple $(\overline{M}, \overline{R})$ for the location of interest. Estimate the spectral value $\varepsilon(T^*)$ for a conditioning period T^* using a representative GMM for the location.

Step 2: Discretize the period range of interest (say, $0.2T_1 - 2T_1$) into $(n-1)$ equally-spaced bins on the log-scale. Include T^* in the discretized set. Thus in (3.5), the variable $\boldsymbol{X_1} \equiv \ln Sa(T_i)$, where $i \in \{1, 2, \ldots, n\}$.

Step 3: Define the target mean conditioned on $\varepsilon(T^*)$ as follows:

$$\boldsymbol{\mu}_{\boldsymbol{\ln Sa}|\,\boldsymbol{\ln Sa(T^*)}} = \begin{bmatrix} \mu_{\ln Sa_{GMM}(T_1)} + \rho_{\varepsilon(T_1),\varepsilon(T^*)}\sigma_{\ln Sa_{GMM}(T_1)}\varepsilon(T^*) \\ \mu_{\ln Sa_{GMM}(T_2)} + \rho_{\varepsilon(T_2),\varepsilon(T^*)}\sigma_{\ln Sa_{GMM}(T_2)}\varepsilon(T^*) \\ . \\ . \\ \mu_{\ln Sa_{GMM}(T_n)} + \rho_{\varepsilon(T_n),\varepsilon(T^*)}\sigma_{\ln Sa_{GMM}(T_n)}\varepsilon(T^*) \end{bmatrix}, \tag{3.6}$$

where $\mu_{\ln Sa_{GMM}(T_i)}$ and $\sigma_{\ln Sa_{GMM}(T_i)}$ are mean and standard deviation of log of $SA(T_i)$ per the GMM, and $\rho_{\varepsilon(T_i),\varepsilon(T^*)}$ is the correlation between spectral ordinate at T_i and T^*. In other words, (3.6) represents the CMS.

Step 4: Following (3.5), the multivariate random normal $\boldsymbol{X_1} \equiv \ln Sa(T_i)$ is conditioned on the spectral acceleration at the conditioning period $\boldsymbol{X_2}$. Thus,

$\boldsymbol{X_2} \equiv \ln Sa(T^*)$. Therefore, we have conditional covariance as:

$$\boldsymbol{\Sigma_{\ln Sa|\ln Sa(T^*)}} = \boldsymbol{\Sigma_{\ln Sa}} - \frac{1}{\sigma^2_{\ln Sa(T^*)}} \boldsymbol{\Sigma_{12|n\times 1}\Sigma_{21|1\times n}}, \tag{3.7}$$

where $\boldsymbol{\Sigma_{\ln Sa}}$ is given by:

$\boldsymbol{\Sigma_{\ln Sa}} =$

$$\begin{bmatrix} \sigma^2_{\ln Sa(T_1)} & \rho_{\varepsilon(T_1),\varepsilon(T_2)}\sigma_{\ln Sa(T_1)}\sigma_{\ln Sa(T_2)} & \cdots & \rho_{\varepsilon(T_1),\varepsilon(T_n)}\sigma_{\ln Sa(T_1)}\sigma_{\ln Sa(T_n)} \\ \rho_{\varepsilon(T_2),\varepsilon(T_1)}\sigma_{\ln Sa(T_2)}\sigma_{\ln Sa(T_1)} & \sigma^2_{\ln Sa(T_2)} & \cdots & \rho_{\varepsilon(T_2),\varepsilon(T_n)}\sigma_{\ln Sa(T_2)}\sigma_{\ln Sa(T_n)} \\ . & . & \cdots & . \\ . & . & \cdots & . \\ \rho_{\varepsilon(T_n),\varepsilon(T_1)}\sigma_{\ln Sa(T_n)}\sigma_{\ln Sa(T_1)} & \rho_{\varepsilon(T_n),\varepsilon(T_2)}\sigma_{\ln Sa(T_n)}\sigma_{\ln Sa(T_2)} & \cdots & \sigma^2_{\ln Sa(T_n)} \end{bmatrix}, \tag{3.8}$$

$\boldsymbol{\Sigma_{12|n\times 1}}$ is simply a vector of the correlation between $\varepsilon(T^*)$ and $\varepsilon(T_i)$, and $\boldsymbol{\Sigma_{21}}$ is the transpose of $\boldsymbol{\Sigma_{12}}$:

$$\boldsymbol{\Sigma_{12}} = \begin{bmatrix} \rho_{\varepsilon(T_1),\varepsilon(T^*)}\sigma_{\ln Sa(T_1)}\sigma_{\ln Sa(T^*)} \\ \rho_{\varepsilon(T_2),\varepsilon(T^*)}\sigma_{\ln Sa(T_2)}\sigma_{\ln Sa(T^*)} \\ \cdots \\ \rho_{\varepsilon(T_n),\varepsilon(T^*)}\sigma_{\ln Sa(T_n)}\sigma_{\ln Sa(T^*)} \end{bmatrix}. \tag{3.9}$$

The conditional variance of random variables $\ln Sa(T_i)$ are the diagonal entries of (3.7). Mathematically,

$$\begin{aligned} \sigma^2_{\ln Sa(T_i)|\ln Sa(T^*)} &= \sigma^2_{\ln Sa(T_i)} - \frac{1}{\sigma^2_{\ln Sa(T^*)}} \left(\rho_{\varepsilon(T_i),\varepsilon(T^*)}\sigma_{\ln Sa(T_i)}\sigma_{\ln Sa(T^*)}\right)^2 \\ &= \sigma^2_{\ln Sa(T_i)} \left(1 - \rho^2_{\varepsilon(T_i),\varepsilon(T^*)}\right). \end{aligned} \tag{3.10}$$

Step 5: Simulate N_0 sets of random arrays following the multivariate lognormal distribution with mean $\boldsymbol{\mu_{\ln Sa|\ln Sa(T^*)}}$ and covariance $\boldsymbol{\Sigma_{\ln Sa|\ln Sa(T^*)}}$ given by (3.6) and (3.7), respectively.

Step 6: Scale all records in the database to match the $Sa(T^*)$ value. The scaling factor

for each record is:

$$scale = \frac{Sa(T^*)}{Sa_{geoMean,k}(T^*)},$$

where $Sa(T^*)$ is the target spectral acceleration and $Sa_{geoMean,k}(T^*)$ is the unscaled spectral acceleration at conditioning period, T^* of k-th record. Filter down the database to contain the time histories that meet the fault mechanism, geotechnical conditions, magnitude-bin, distance-bin, local site conditions, scaling limits, etc.

Step 7: Each of the N_0 simulated response spectra is compared with the every time-history record in the pruned database to find the best match. The best match is defined by the minimum SSE_k value defined in (3.4). At the end of this step, N_0 records having optimal individual matches with the simulated multivariate spectral ordinates are obtained.

Step 8: Since the error in time-history is minimized individually in the previous step, the statistics of the selected records may accumulate errors resulting in a mismatch between the sample statistics and the targeted statistics, $\boldsymbol{\mu}_{\ln Sa|\ln Sa(T^*)}$, $\boldsymbol{\Sigma}_{\ln Sa|\ln Sa(T^*)}$. To fine-tune the selected ground motion set, a greedy algorithm is employed (Baker, 2011). Each individually-optimal N_0 record is attempted to replace one of the remaining ground motions such that the revised sample is close to the target statistics. A penalty function using the weighted sum of differences between sample and target statistics is defined for optimization.

It is worth noting that the selected set of site- and structure-specific time histories is suitable when used collectively and not individually.

3.2.3 Earthquake Databases for Ground Motion Selection

Characteristics of recorded earthquakes in the database are required to reflect the tectonic features of the location of interest. The process of ground motion selection involves filtering based on a range of earthquake characteristics, such as magnitude, distance, geotechnical characteristics, and fault mechanism. Scaling a recorded time history to match a target spectrum beyond a limit can result in biased estimates of structural capacity. Excessively scaled smaller events fail to capture the frequency

characteristics of large earthquakes. The available data for large Cascadia earthquakes are scarce. The higher frequency of major earthquakes near Japan and a large network of recording stations have resulted in a reliable strong-motion database (Goda and Atkinson, 2009). The database based on the Kyoshin and Kiban-Kyoshin network (K-NET and KiK-net) for Japanese earthquakes (NIED, 2019) is a useful resource for ground motion selection, especially in southwestern Canada.

PEER NGA-West2 Database NGA-West project (Chiou et al., 2008) was developed by PEER with contributions from several organizations. The dataset contained 3,551 time-history records with multiple components during 173 Shallow Crustal earthquakes of magnitude 4.2 to 7.9 at Joyner-Boore distance (R_{JB}) from 0 to 472.6 km. The NGA-West database was extensively expanded in 2014 as NGA-West2 (Ancheta et al., 2014). The updated database contains a total of 21,539 records from 599 earthquakes, including several small and moderate earthquakes in addition to large earthquakes, thus broadening the range of magnitudes from 3.0 to 7.9. NGA-West2 database contains 10,792 recordings from events with $M \in [3.0, 4.5]$. Metadata containing the spectral metadata is available for the database, thus facilitating the ground motion selection. The metadata provides the elastic spectral ordinates for different damping ratios in addition to various characteristics of the earthquake and recording station, such as magnitude, Joyner-Boore distance, faulting mechanism, the closest distance to the ruptured area, and shear wave velocity in the top 30 m soil (V_{s30}). Thus, the metadata allows the search for ground motion records without the need for processing the complete time history for such a large database. In the NGA-West2 database, fault mechanism is denoted by 0 for Strike-Slip, 1 for Normal, 2 for Reverse, 3 for Reverse Oblique, 4 for Normal Oblique, and -999 for unknown mechanism. The numbers of earthquakes with strike, normal, and reverse slip mechanisms are 327 (54%), 112 (19%), and 148 (25%), respectively.

Metadata for KiK-net databas In the aftermath of the 1995 Kobe earthquake, the Kyoshin network (K-NET) and Kiban-Kyoshin network (KiK-net) database (2019) were set up across Japan. The K-NET/KiK-net consists of a widespread network of approximately 1,000 stations. Site classification for the database has been investigated in the literature in great detail (Cabas et al., 2017; Bahrampouri et al., 2021; Pilz and Cotton, 2019; Zhu et al., 2021). These databases witnessed an exponential growth in the high-quality data from the 2011 M9 Tohoku earthquake when over 1000

recordings were collected. Numerous aftershocks further consolidated the database and uncovered an understanding of the spatial distribution of large seismic events. The Tohoku earthquake database is used in the present study to select the Cascadian earthquake due to their anticipated similarity between the subduction fault rupture mechanism of two regions (Tesfamariam and Goda, 2015; Goda et al., 2015).

The KiK-net database is one of the most treasured strong ground motion databases and is open to the public. However, the records are uploaded in a raw format, and important metadata associated with the records is not provided. Hence, the metadata and processing of records are necessary before they can be used for engineering applications. In the present section, we discuss the details of metadata for KiK-net records.

Each of the 650+ KiK-net sites has two seismographs, one at a borehole installed typically at 100 to 250 m of depth and another at the surface. Each KiK-net recordings have six channels; the first three correspond to a borehole seismograph and have file extension as `NS1`, `EW1`, and `UD1`, the next three correspond to a surface seismograph and have file extensions of `NS2`, `EW2`, and `UD2`. `NS` and `EW` indicate horizontal records of the seismographs whereas `UD` indicates the vertical direction. KiK-net recordings have three channels with extensions `NS`, `EW`, and `UD`. The flat-file of response spectra for the Japanese database was developed by Dawood et al. (2016) for the records until 2015. This flat-file consisted of 56,473 strong ground motion records from 4021 earthquakes. Bahrampouri and Rodriguez-Marek (2019) updated that database to contain all earthquakes with $M_w > 3$ and recorded between Oct 1997 and the end of 2017. The updated database has 222,688 records from 10,552 earthquakes. They also compiled comprehensive metadata for each record. Earthquakes are classified based on tectonics into *Shallow Crustal* or *subduction zone* (which is further subdivided into Interface, intraslab, upper mantle, and outer subduction) earthquakes following the criteria given by Garcia et al. (2012) and Zhao et al. (2015). They also classified earthquakes based on the faulting mechanism into *reverse*, *strike slip*, *normal*, and unknown type, following the algorithms by Frohlich (1992) and Kagan (2002). Table 3.1 shows the statistics of the tectonic region and fault mechanism of recorded earthquake events in the KiK-net database.

A new metadata file is generated for all recordings of KiK-net so as to make the variable names and information consistent with NGA-West2 metadata. The variables

Table 3.1: Distribution of events in KiK-net into different tectonic regime and fault mechanism.

Tectonic Regime	Fault Mechanism				Sum
	Reverse (1)	Strike (2)	Normal (3)	Unknown (−99)	
Interface (1)	1,469	–	–	121	1,590 (15%)
Shallow crustal (2)	920	396	565	665	2,546 (24%)
Intra-slab (3)	524	153	388	786	1,851 (18%)
Upper mantle (4)	–	–	–	–	– (0%)
Outer subduction (5)	6	154	73	120	353 (3%)
Unknown (−99)	–	–	–	4,212	4,212 (40%)
				Total	**10,552**

Numbers in the parentheses followed by the tectonic regime or fault mechanism correspond to the identifiers in the database.

contained in the developed metadata are explained below. Each recording is stored hierarchically using keys based on the *event*, *site*, and *component*. Highlights of the developed metadata are given below:

1. *Event key* denotes the unique event and is the outermost key. It consists of the event timestamp, e.g., `19980112145100` for the event initiated at the timestamp of 12 Jan 1998, 14:51:00.

2. *Site key* constitutes of station number as its first six bits (e.g., `AICH05`) followed by the recording time (e.g., `9801121451` for the timestamp of 12 Jan 1998, 14:51). An example site key is `AICH059801121451`. The site key is unique to each recording.

3. *Component key* refers to one of the six recorded components on each station. The two horizontal components recorded by the surface seismograph are denoted by `NS2` and `EW2`, whereas the horizontal component recordings on the borehole seismograph are stored with keys `NS1` and `EW1`.

4. *Earthquake information*: Variables are stored containing the information of hypocenter and recording station location (latitude and longitude), magnitude, Joyner-Boore distance, and V_{s30} of soil.

5. *Tectonic regime* and *fault mechanism* are stored per the definitions by Garcia et al. (2012). In the KiK-net database, for the tectonic regime, an indicator variable is assigned as follows: 1 for interface, 2 for shallow crustal, 3 for intraslab, 4 for upper mantle (no records), 5 for outer subduction, and −99 for unknown. Similarly, for the focal mechanism, the assignment is 1 for reverse slip, 2 for strike-slip, 3 for normal slip, and -99 for unknown.

3.3 Example Application of Ground Motion Selection based on NBCC 2020

This section contains the example of ground motion selection for Vancouver City Hall when a conditional spectrum is targeted with a conditioning period of 1.5 s. As shown in Tables 2.1, three distinct kinds of seismic events—crustal, interface, and instraslab—can be critical depending on the intensity measure of interest. While the NGA-West database comprises global Shallow Crustal earthquakes, the KiK-net database has records from shallow crustal and subduction earthquakes. The range of magnitudes is limited to ± 1.5 from the disaggregated magnitudes. A distance of 20 km is set as a minimum to exclude near-field records. To limit the bias in the estimated structural response introduced by excessive scaling of the recorded ground motion, a limit of 5 is imposed on the scaling Watson-Lamprey and Abrahamson (2006); Luco and Bazzurro (2007). In the next chapter, the results of ground motion selection for this example along with the effects of different parameters, are presented.

Chapter 4

Parametric Study of Ground Motion Selection

In the present chapter, parametric studies are carried out to investigate their effects on ground motion selection. A total of 30 pairs of ground motion records are selected for each case targeted at the hazard and disaggregation corresponding to Vancouver City Hall. Table 4.1 summarizes the baseline values and variations for different parameters considered in the study. Figure 4.1 shows the results of the baseline case. Each section shows the selected GM suite corresponding to variation in the specific parameter. All other parameters, unless specified, are kept the same as the baseline case. Further, each figure in the present chapter has three subfigures similar to Figure 4.1.

Table 4.1: Parametric study on ground motion selection based on NBC 2020.

Parameter	**Baseline**	**Variation**
Conditioning Period (s)	1.5	1, 3
Period Range	[0.2, 3.0]	[0.5, 3.0], [0.2, 4.5]
Target Mean*	CMS	UHS
Target Return Period	2475	475, 4975
Near-Field Records	$d_{rup} \geq 20$ km	$d_{rup} \geq 5$ km
Scaling Permitted	Yes	No
Scaling Limits	5	10, 2

* Only means are targeted for this variation.

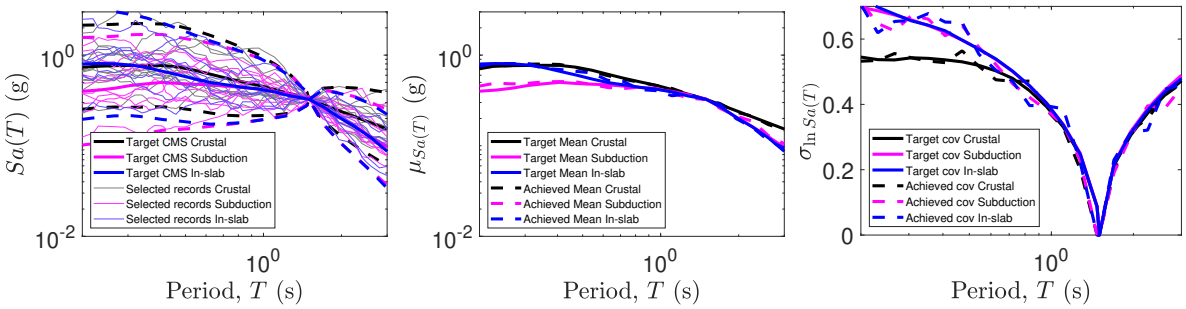

(a) (b) (c)

Figure 4.1: Baseline case. (a) Pseudo-response spectra of individual records, while thick broken lines mark the 97.5%ile and 2.5%ile values, (b) target and achieved conditional mean for the three tectonic regimes, and (c) target and achieved log-standard deviation for the conditional spectra. See Table 4.1 for details of ground motion selection parameters.

4.1 Effects of Conditioning Period on Ground Motion Selection

Figures 4.2 and 4.3 show the selected ground motion suite when the conditioning period is changed to 1.0 s and 3.0 s instead of the baseline value of 1.5 s. In case of $T^* = 3.0$ s, $2T^*$ exceeds the maximum period of some GMM (e.g., Zhao et al. (2006) is defined for periods up to 5 s), extrapolation using the ratio of corresponding spectral acceleration in AB03 Atkinson and Boore (2003) is employed as suggested by Kolaj et al. (2019).

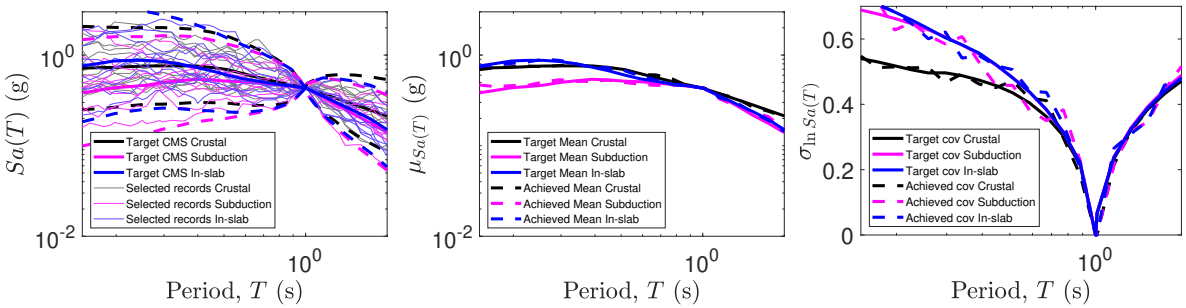

(a) (b) (c)

Figure 4.2: Effect of the conditioning period $T^* = 1.0$ s. Accordingly, the target period range is [0.15 s, 2.0 s]. All other parameters are kept the same as baseline (Table 4.1).

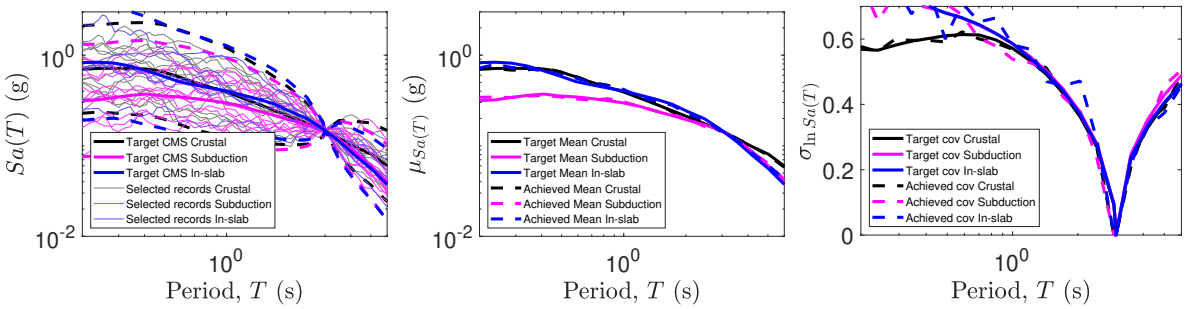

(a) (b) (c)

Figure 4.3: Effect of the conditioning period $T^* = 3.0$ s. Accordingly, the target period range is [0.2 s, 6.0 s]. All other parameters are kept the same as baseline (Table 4.1).

4.2 Effects of Period Range

Figure 4.4 shows the selected ground motion records when the lower bound of the target period range is increased to 0.5 s from 0.2 s of the basline. Whereas, Figure 4.5 shows the case when the upper limit is increased fro 4.5 s from 3.0 s.

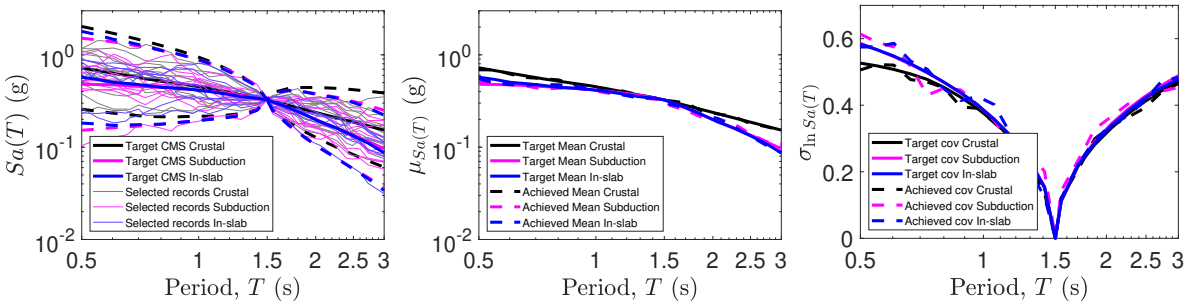

(a) (b) (c)

Figure 4.4: Effect of the lower bound in the target period range with a target of [0.5 s, 3.0 s]. All other parameters are kept the same as baseline (Table 4.1).

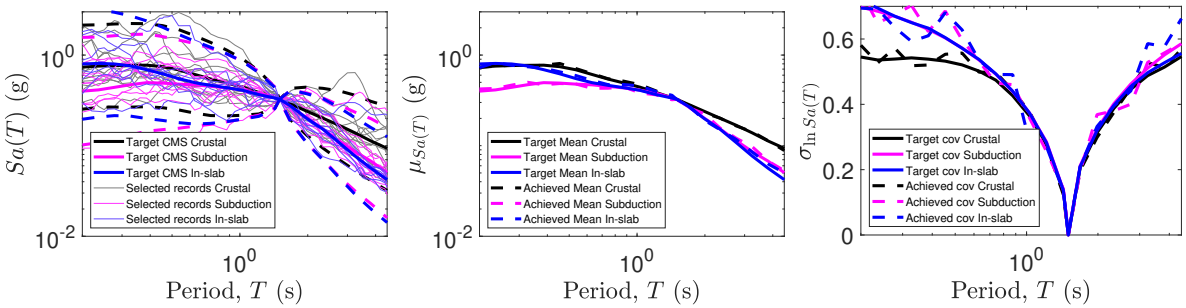

(a) (b) (c)

Figure 4.5: Effect of the upper bound in the target period range with a target of [0.2 s, 4.5 s]. All other parameters are kept the same as baseline (Table 4.1).

4.3 Effect of Target Spectrum

Figures 4.6 and 4.7 show the selected ground motion records when only CMS and only UHS are targeted, respectively. It is worth noting that the covariances of spectral accelerations are not targeted in these cases. Therefore, the target vector of $\sigma_{\ln Sa(T)}$ in both figures are zero for all periods.

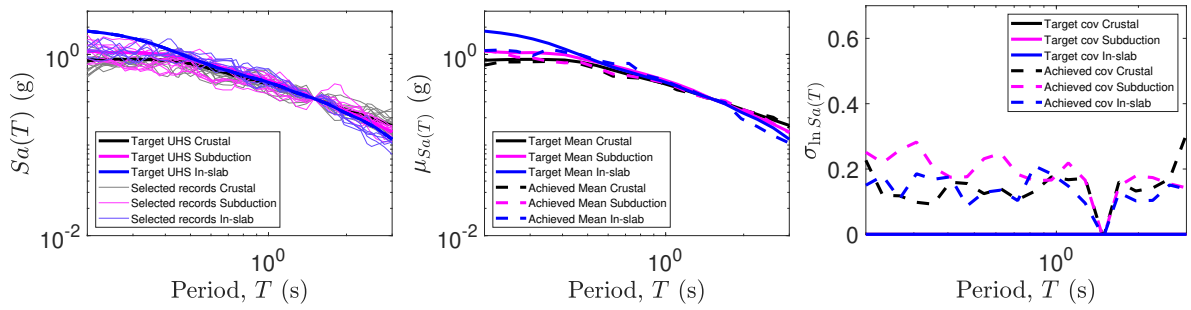

(a) (b) (c)

Figure 4.6: Effect of the targeting CMS only. All other parameters are kept the same as baseline (Table 4.1).

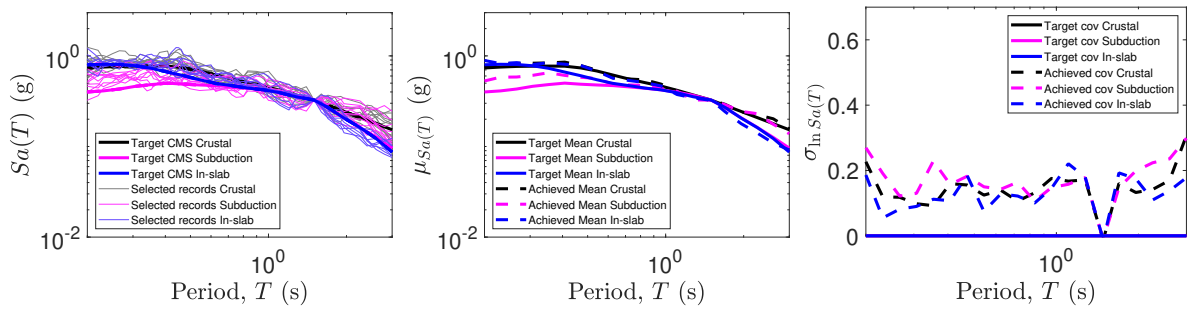

(a) (b) (c)

Figure 4.7: Effect of the targeting UHS only. All other parameters are kept the same as baseline (Table 4.1).

4.4 Effect of Return Period

Figure 4.8 and 4.9 show the selected ground motion records when the return period for target spectra are considered as 475 and 4975 years, respectively. It is noted that the target hazard and disaggregation are both considered corresponding to those return periods.

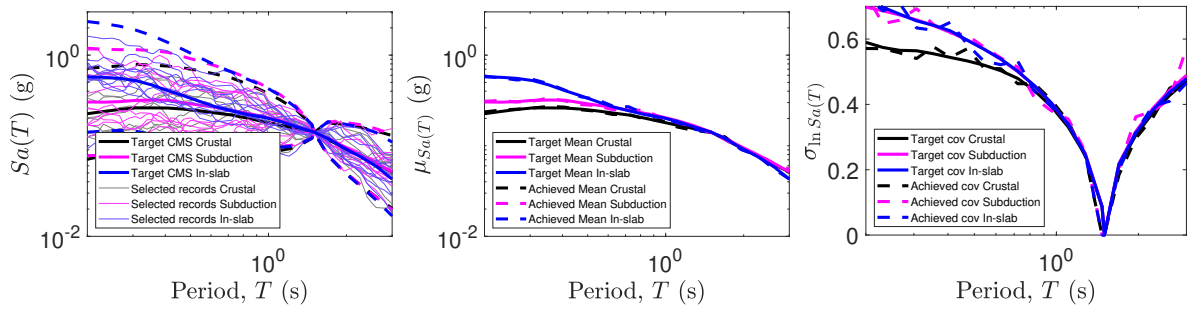

(a) (b) (c)

Figure 4.8: Effect of the return period of 475 years for target spectrum. All other parameters are kept the same as baseline (Table 4.1).

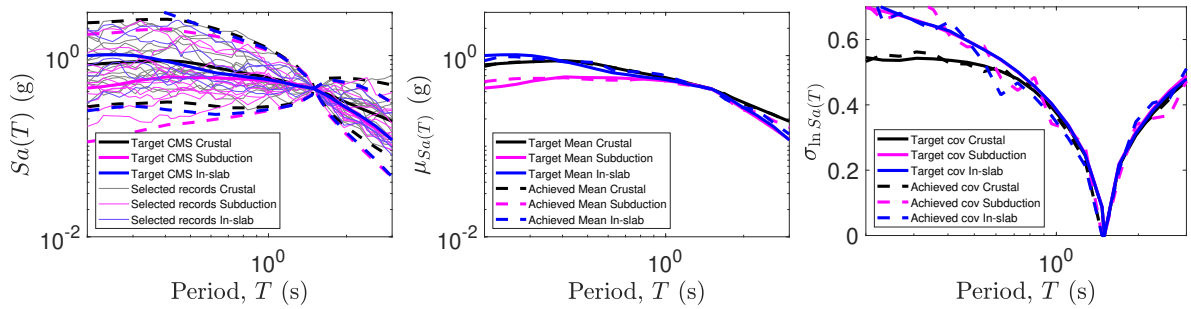

(a) (b) (c)

Figure 4.9: Effect of the return period of 4975 years for target spectrum. All other parameters are kept the same as baseline (Table 4.1).

4.5 Near-Fault Ground Motion Selection

Figure 4.10 shows the selected groun motion records when the near-field ground motions are allowed and a distance $d_{rup} \geq 5$ km is imposed comapred to $d_{rup} \geq 20$ km for the baseline.

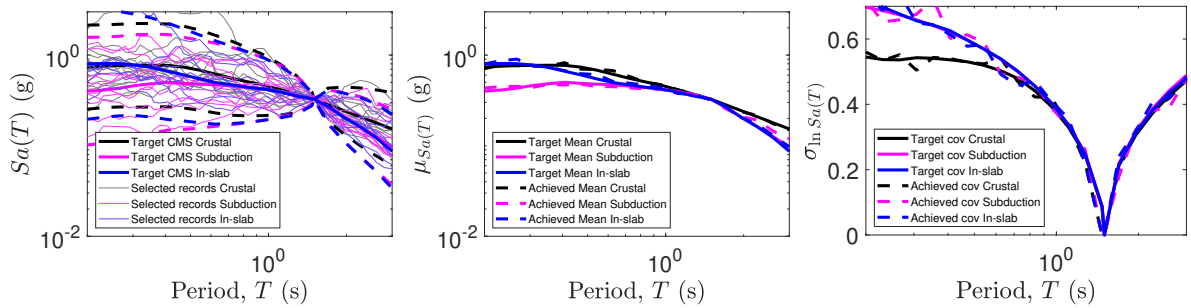

(a) (b) (c)

Figure 4.10: Effect of allowing near-field records ($d_{rup} \geq 5$ km). All other parameters are kept the same as baseline (Table 4.1).

4.6 Effect of not Allowing Scaled Ground Motion Records

Figure 4.11 shows the effect of not allowing the scaling of ground motion records. A band near the conditioning period rather than a constant value, as in all other cases, is observed. Similarly, the values of $\sigma_{\ln Sa(T^*)}$ is not zero.

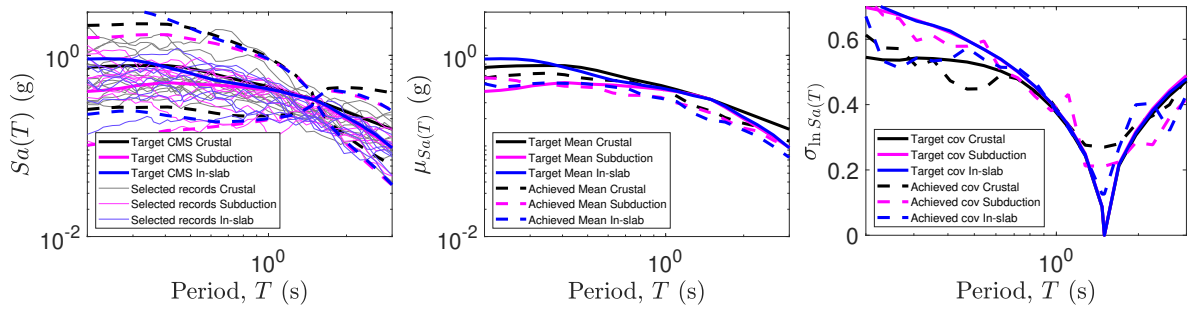

(a) (b) (c)

Figure 4.11: Effect of not allowing the scaling of records in the databases. All other parameters are kept the same as baseline (Table 4.1).

4.7 Effect of Limits on Scaling of Ground Motion Records

Figures 4.12 and 4.13 show the selected ground motion records when the scaling factor is limited to 10 and 2, respectively. A better match for both median, as well as standard deviation is observed when higher scaling is permitted.

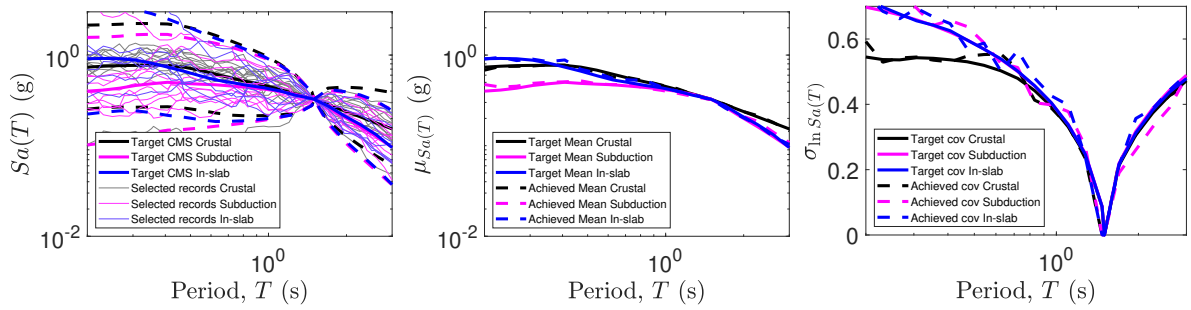

(a) (b) (c)

Figure 4.12: Effect of the maximum permissible scaling of records of 10 in the databases. All other parameters are kept the same as baseline (Table 4.1).

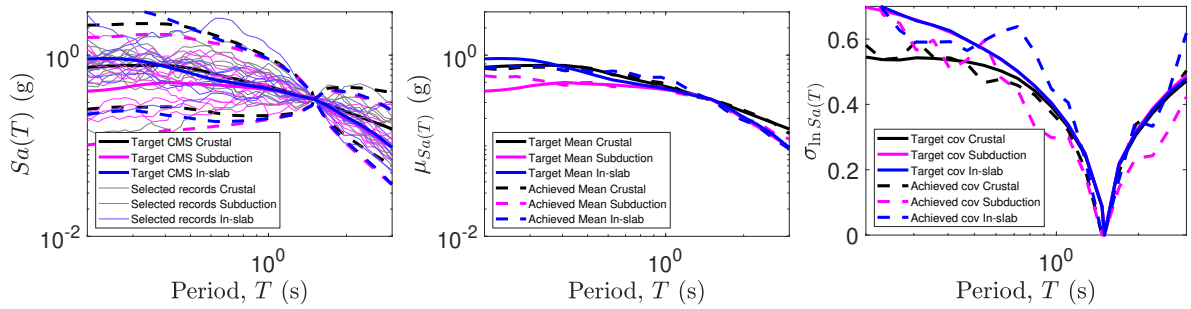

(a) (b) (c)

Figure 4.13: Effect of the maximum permissible scaling of records of 2 in the databases. All other parameters are kept the same as baseline (Table 4.1).

4.8 SDOF Response with Peak-Oriented IMK Hysteresis

In the present section, we investigate the effects of different ground motion suites developed in the previous sections on an idealized single-degree-of-freedom (SDOF) system with peak-oriented Ibarra-Medina-Krawinkler (IMK, Ibarra et al., 2005) hysteresis response. This model has been widely used for modeling different types of structural systems (Liel et al., 2009; Haselton et al., 2011; Lignos and Krawinkler, 2011; Noh et al., 2017). The IMK model has been shown to capture strength and stiffness degradation along with in-cycle and cyclic deterioration. The model has a characteristic negative slope helpful in capturing the collapse. The present study adopts the reference case from Baltzopoulos et al. (2018). These parameters are listed in Table 4.2. `ModIMKPeakOriented` uniaxial material in `OpenSees` was used in the present study. A Rayleigh damping of 5% is considered for the model.

Incremental Dynamic Analysis (IDA, Vamvatsikos and Cornell, 2002) is carried out on the selected SDOF system using each ground motion suite. Figures 4.14 to 4.26 show IDA curves and collapse fragility for the SDOF hysteretic system corresponding to each ground motion suite. Table 4.3 shows the collapse fragility parameters for different GM suites. Among all considered variations, the effects of the conditioning period (T^*) and the restriction on scaling are most pronounced. They both reduce the assessed median collapse capacity.

Table 4.2: Peak-oriented modified IMK hysteresis model parameters adopted in the present study.

Parameter	Description	Value
K_e	Elastic stiffness	3142.9 kN/m
$\delta_{p,+}$	Pre-capping deformation in positive loading direction	0.49 m
$\delta_{pc,+}$	Post-capping deformation in positive loading direction	0.19 m
$\delta_{u,+}$	Ultimate deformation in positive loading direction	0.75 m
$F_{y,+}$	Yield strength in positive loading direction	2200 kN
$F_{max,+}/F_{y,+}$	Maximum-to-yield strength ratio in positive loading direction	1.084
$F_{res,-}/F_{y,+}$	Residual-to-yield strength ratio in positive loading direction	0
$\delta_{p,-}$	Pre-capping deformation in negative loading direction	0.35 m
$\delta_{pc,-}$	Post-capping deformation in negative loading direction	0.19 m
$\delta_{u,-}$	Ultimate deformation in negative loading direction	-0.61 m
$F_{y,-}$	Yield strength in negative loading direction	1900 kN
$F_{max,-}/F_{y,-}$	Maximum-to-yield strength ratio in negative loading direction	1.072
$F_{res,-}/F_{y,-}$	Residual-to-yield strength ratio in negative loading direction	0
λ_S	Cyclic deterioration parameter for yield strength deterioration	1500
λ_C	Cyclic deterioration parameter for post-capping stiffness deterioration	1500
λ_A	Cyclic deterioration parameter for accelerated reloading stiffness deterioration	1500
λ_K	Cyclic deterioration parameter for unloading stiffness deterioration	1500
c_S	Rate of yield strength deterioration	1
c_C	Rate of post-capping stiffness deterioration	1
c_A	Rate of accelerated reloading stiffness deterioration	1
c_K	Rate of unloading stiffness deterioration	1
D_+	rate of cyclic deterioration in the positive loading direction; = 1 for symmetric hysteretic response.	1
D_-	rate of cyclic deterioration in the negative loading direction; = 1 for symmetric hysteretic response.	1

Table 4.3: Collapse fragility parameters of SDOF system using different bases of GM suite selection.

Case	$\mu_{Sa(T),collapse}$ (g)	$\beta_{\ln,collapse}$
Baseline	0.943	0.484
Effect of the conditioning period $T^* = 1.0$ s	1.016	0.425
Effect of the conditioning period $T^* = 3.0$ s	0.720	0.414
Smaller lower bound in the target period range	1.037	0.474
Higher upper bound in the target period range	0.913	0.440
Targeting CMS only	0.920	0.465
Targeting UHS only	0.925	0.442
$T_R = 475$ years for target spectrum	0.984	0.498
$T_R = 4975$ years for target spectrum	0.943	0.445
Near-field records	0.967	0.455
Scaling not allowed	0.862	0.462
Scaling allowed up to 10	1.028	0.469
Scaling allowed up to 2	0.974	0.474

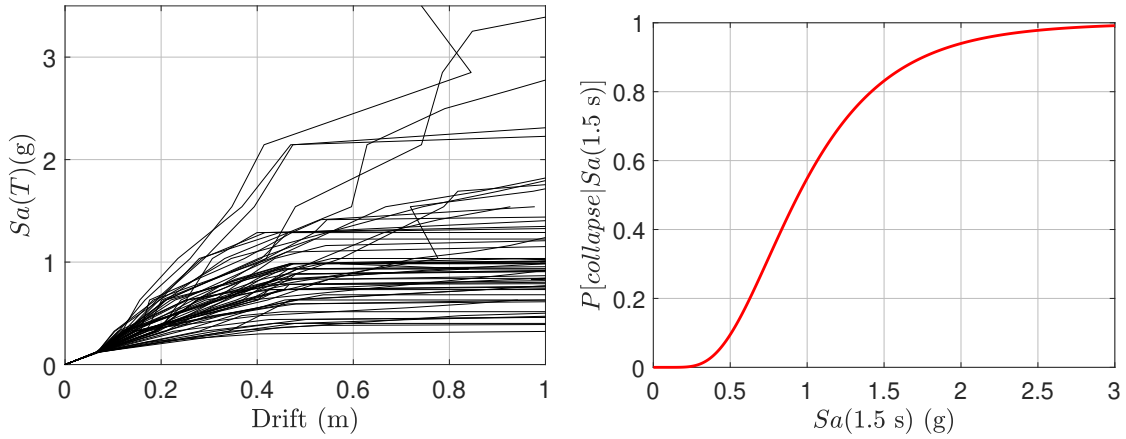

(a) (b)

Figure 4.14: Baseline case. (a) IDA curves and (b) collapse fragility. See Table 4.1 for details of ground motion selection parameters.

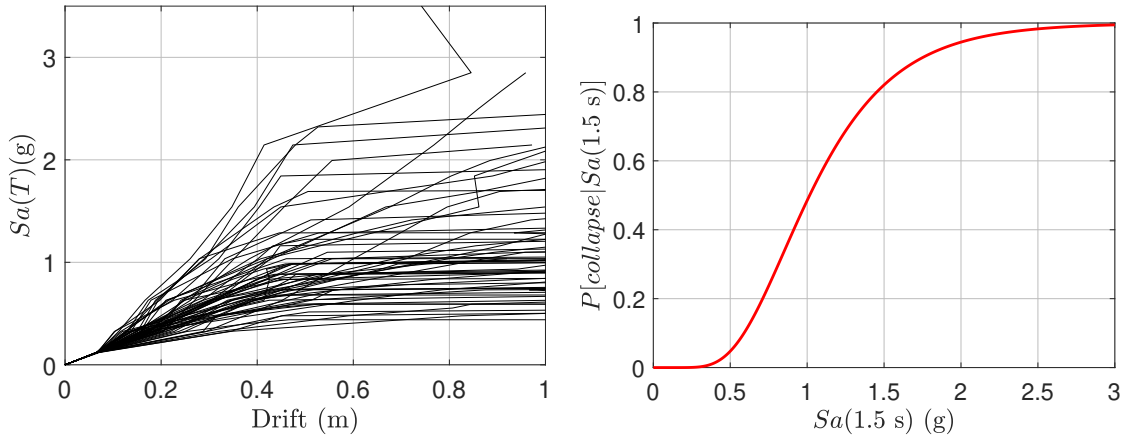

(a) (b)

Figure 4.15: (a) IDA curves and (b) collapse fragility. Effect of the conditioning period $T^* = 1.0$ s. Accordingly, the target period range is [0.15 s, 2.0 s]. All other parameters are kept the same as baseline (Table 4.1).

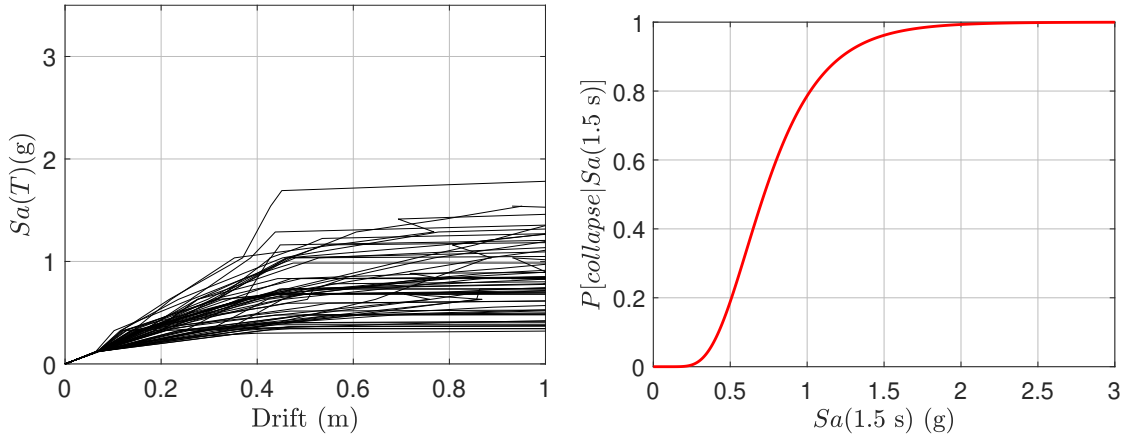

(a) (b)

Figure 4.16: (a) IDA curves and (b) collapse fragility. Effect of the conditioning period $T^* = 3.0$ s. Accordingly, the target period range is [0.2 s, 6.0 s]. All other parameters are kept the same as baseline (Table 4.1).

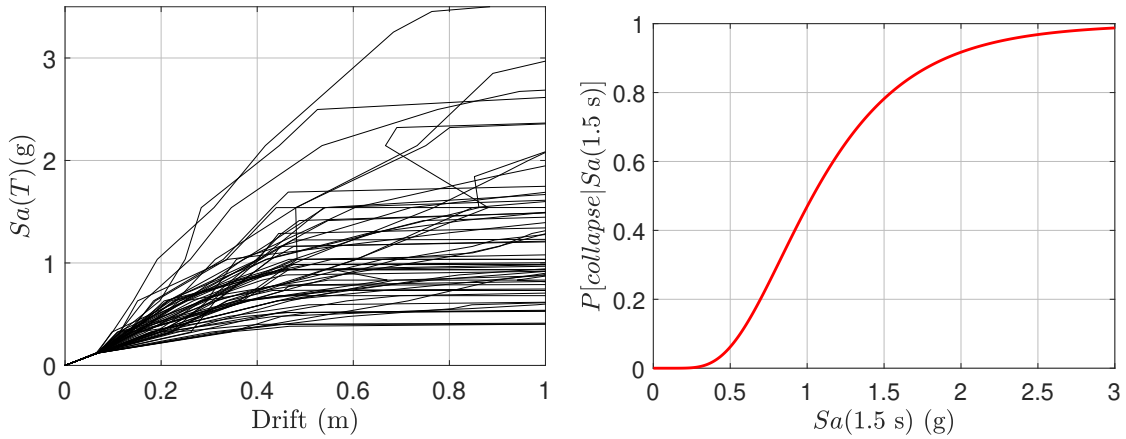

(a) (b)

Figure 4.17: (a) IDA curves and (b) collapse fragility. Effect of the lower bound in the target period range with a target of [0.5 s, 3.0 s]. All other parameters are kept the same as baseline (Table 4.1).

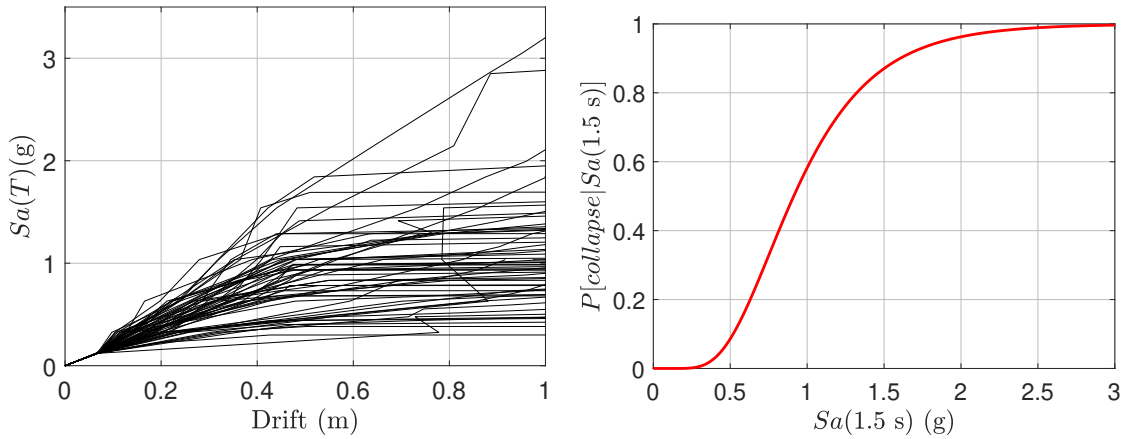

(a) (b)

Figure 4.18: (a) IDA curves and (b) collapse fragility. Effect of the upper bound in the target period range with a target of [0.2 s, 4.5 s]. All other parameters are kept the same as baseline (Table 4.1).

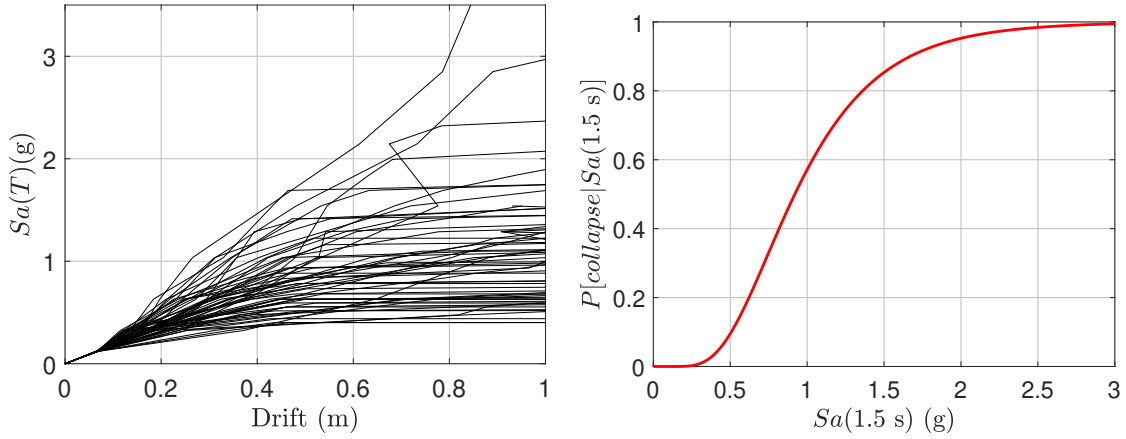

(a) (b)

Figure 4.19: (a) IDA curves and (b) collapse fragility. Effect of the targeting CMS only. All other parameters are kept the same as baseline (Table 4.1).

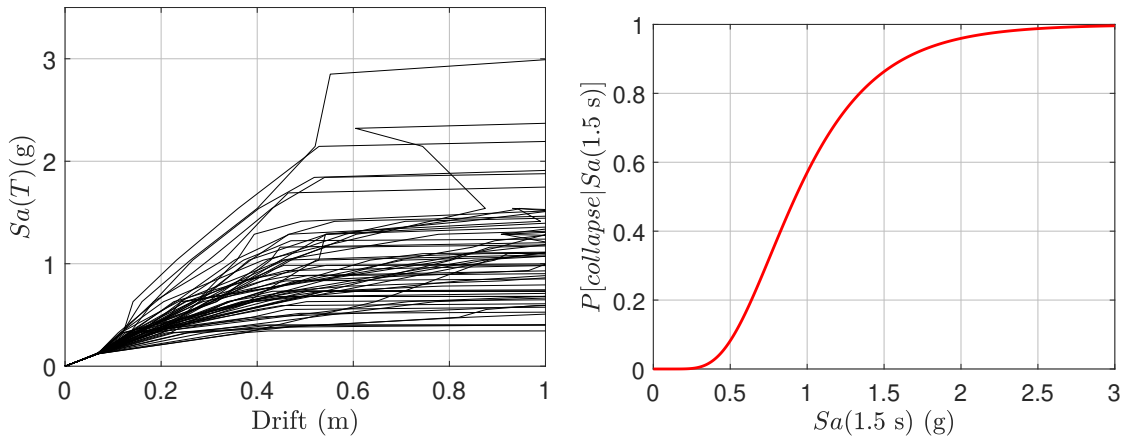

(a) (b)

Figure 4.20: (a) IDA curves and (b) collapse fragility. Effect of the targeting UHS only. All other parameters are kept the same as baseline (Table 4.1).

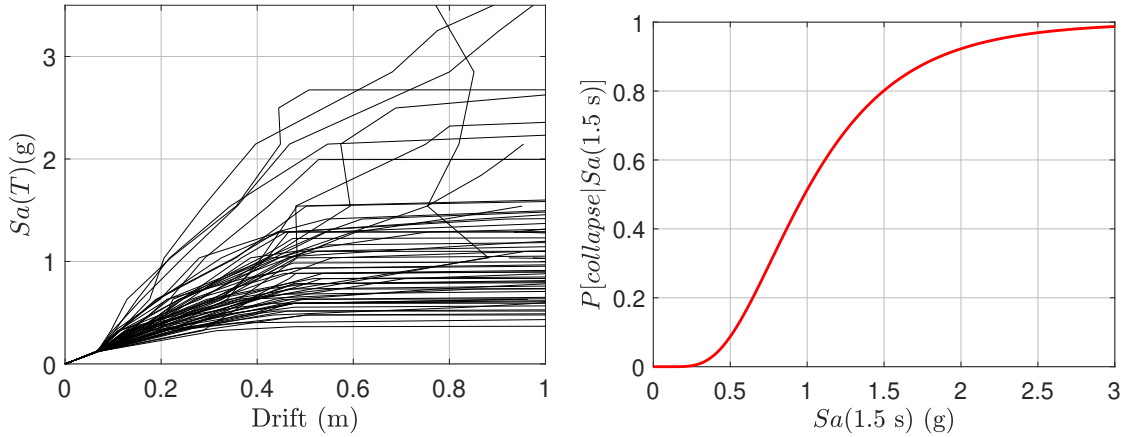

(a) (b)

Figure 4.21: (a) IDA curves and (b) collapse fragility. Effect of the return period of 475 years for target spectrum. All other parameters are kept the same as baseline (Table 4.1).

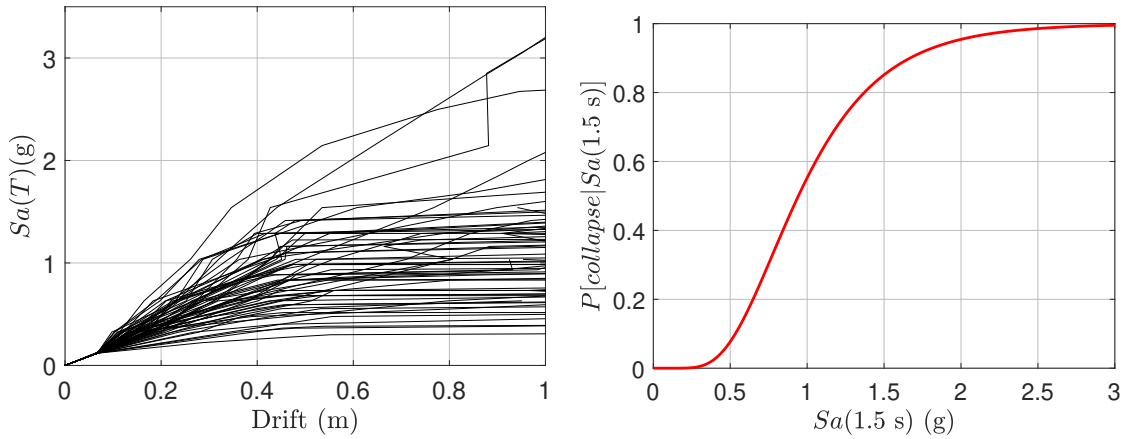

(a) (b)

Figure 4.22: (a) IDA curves and (b) collapse fragility. Effect of the return period of 4975 years for target spectrum. All other parameters are kept the same as baseline (Table 4.1).

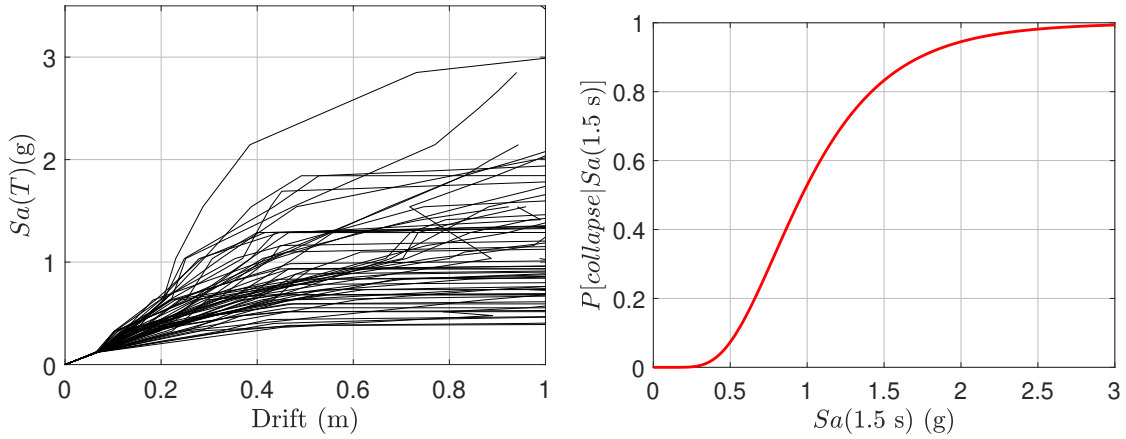

(a) (b)

Figure 4.23: (a) IDA curves and (b) collapse fragility. Effect of allowing near-field records ($d_{rup} \geq 5$ km). All other parameters are kept the same as baseline (Table 4.1).

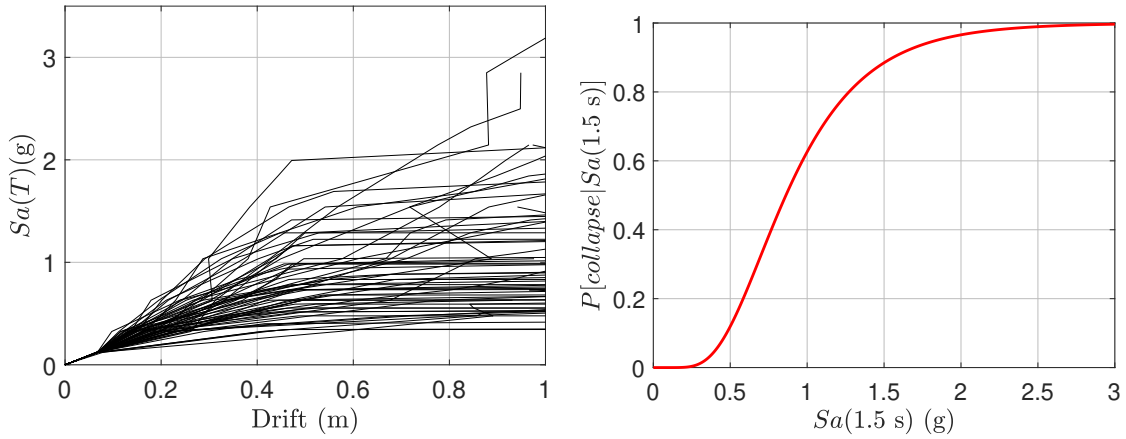

(a) (b)

Figure 4.24: (a) IDA curves and (b) collapse fragility. Effect of not allowing the scaling of records in the databases. All other parameters are kept the same as baseline (Table 4.1).

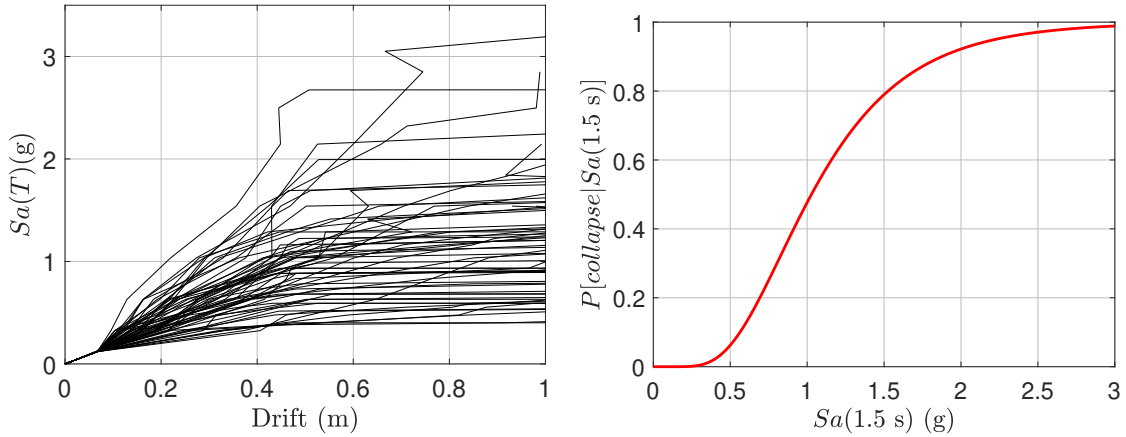

(a) (b)

Figure 4.25: (a) IDA curves and (b) collapse fragility. Effect of the maximum permissible scaling of records of 10 in the databases. All other parameters are kept the same as baseline (Table 4.1).

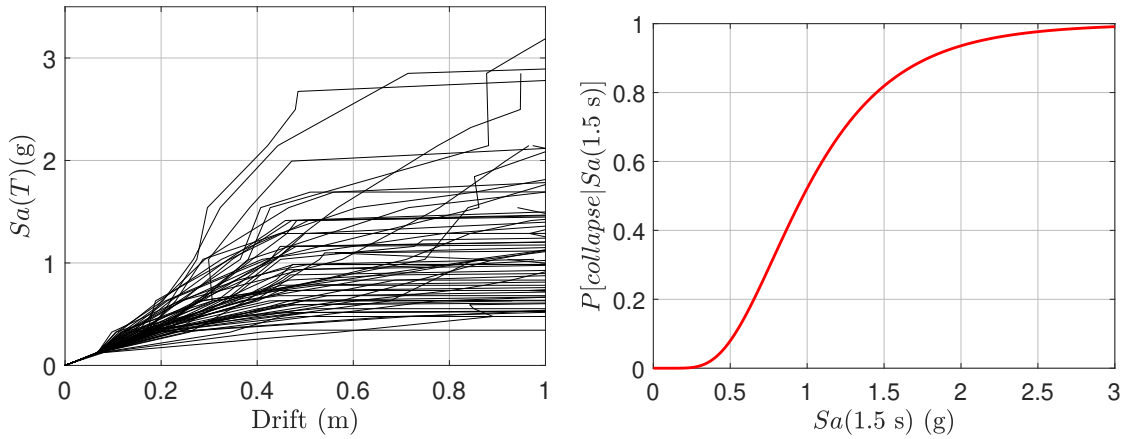

(a) (b)

Figure 4.26: (a) IDA curves and (b) collapse fragility. Effect of the maximum permissible scaling of records of 2 in the databases. All other parameters are kept the same as baseline (Table 4.1).

Chapter 5

Conclusions

The present report provides a methodology for ground motion selection consistent with the latest sixth seismic hazard model of Canada. The study built up on the NRCan's `OpenQuake` models and laid out detailed steps for the probabilistic seismic hazard analysis, including the characteristics of the site and intensity measure of interest. The intensity measure is expected to capture the buildings subjected to nonlinear time history. The major conclusions of the present study are:

- The latest hazard model leads to a significant increase in the estimates of seismicity for several locations in Canada. The report illustrated the assessment of these latest estimates. The median hazard curve and uncertainties associated with it are estimated. Disaggregation charts are developed to ascertain the highest contributing sources and scenarios.
- A hazard-consistent ground motion selection procedure is explained, and in-house tools for selection are developed.
- The developed methodology allows for the site- and structure-specific ground motion selection that respects the seismotectonic features of a site. As an example location, Vancouver City Hall, with a complex seismicity consisting of Crustal, Subduction, and In-slab tectonic regimes, is considered. International strong-motion databases of NGA-West2 and KiK-net (Ancheta et al., 2014; NIED, 2019) are used to appropriately capture ground motion records generated in different tectonics.
- A parametric study is carried out to ascertain the effects of different inputs,

such as the conditioning period, targeted period range, and the return period of interest, on the ground motion selection.

- A simplified SDOF hysteretic model following peak-oriented Ibarra-Medina-Krawinkler hysteresis rules is considered to carry out incremental dynamic analysis using different ground motion suites.
- Among different variations considered for the ground motion selection, the effects of the conditioning period and the restriction on scaling are most significant. They both reduce the assessed median collapse capacity.

The report is the first attempt of its kind that is based on the latest National Building Code of Canada, NBC 2020 (2022). In future investigations, the impact of different ground motion suites on the full-scale building response can be undertaken. Further, ground motion selection using vector intensity measures can also be carried out.

References

Abrahamson, N., Gregor, N., and Addo, K. (2016). BC Hydro ground motion prediction equations for subduction earthquakes. *Earthquake Spectra*, 32(1):23–44.

Abrahamson, N. and Silva, W. (2008). Summary of the Abrahamson & Silva NGA ground-motion relations. *Earthquake spectra*, 24(1):67–97.

Abrahamson, N. and Silva, W. J. (1997). Empirical response spectral attenuation relations for shallow crustal earthquakes. *Seismological Research Letters*, 68(1):94–127.

Abrahamson, N. A., Silva, W. J., and Kamai, R. (2014). Summary of the ASK14 ground motion relation for active crustal regions. *Earthquake Spectra*, 30(3):1025–1055.

Adams, J., Allen, T., Halchuk, S., and Kolaj, M. (2019). Canada's 6th generation seismic hazard model, as prepared for the 2020 National Building Code of Canada. In *12th Canadian Conference on Earthquake Engineering*.

Ancheta, T. D., Darragh, R. B., Stewart, J. P., Seyhan, E., Silva, W. J., Chiou, B. S.-J., Wooddell, K. E., Graves, R. W., Kottke, A. R., Boore, D. M., et al. (2014). NGA-West2 database. *Earthquake Spectra*, 30(3):989–1005. https://doi.org/10.1193/070913EQS197M https://peer.berkeley.edu/ngawest2/databases.

ASCE 7 (2010). Minimum design loads for buildings and other structures (ASCE/SEI 7-10). *American Society of Civil Engineers, Reston, Virginia*.

ASCE 7 (2016). Minimum design loads for buildings and other structures (ASCE/SEI 7-16). *American Society of Civil Engineers, Reston, Virginia*.

ATC 40 (1996). Seismic evaluation and retrofit of concrete buildings. *Applied Technology Council, report ATC-40. Redwood City*.

Atkinson, G. M. and Boore, D. M. (2003). Empirical ground-motion relations for

subduction-zone earthquakes and their application to Cascadia and other regions. *Bulletin of the Seismological Society of America*, 93(4):1703–1729.

Atkinson, G. M. and Macias, M. (2009). Predicted ground motions for great interface earthquakes in the Cascadia subduction zone. *Bulletin of the Seismological Society of America*, 99(3):1552–1578.

Bahrampouri, M. and Rodriguez-Marek, A. (2019). Ground motion parameters for KiK-net records: An updated database. *DesignSafe-CI*. https://doi.org/10.17603/ds2-e0ts-c070.

Bahrampouri, M., Rodriguez-Marek, A., Shahi, S., and Dawood, H. (2021). An updated database for ground motion parameters for KiK-net records. *Earthquake Spectra*, 37(1):505–522.

Baker, J., Bradley, B., and Stafford, P. (2021). *Seismic hazard and risk analysis*. Cambridge University Press.

Baker, J. W. (2011). Conditional mean spectrum: tool for ground-motion selection. *Journal of Structural Engineering*, 137(3):322–331.

Baker, J. W. and Jayaram, N. (2008). Correlation of spectral acceleration values from NGA ground motion models. *Earthquake Spectra*, 24(1):299–317.

Baltzopoulos, G., Baraschino, R., Iervolino, I., and Vamvatsikos, D. (2018). Dynamic analysis of single-degree-of-freedom systems (DYANAS): A graphical user interface for OpenSees. *Engineering Structures*, 177:395–408.

Bazzurro, P. and Cornell, C. A. (1999). Disaggregation of seismic hazard. *Bulletin of the Seismological Society of America*, 89(2):501–520.

Bommer, J. J. and Scherbaum, F. (2008). The use and misuse of logic trees in probabilistic seismic hazard analysis. *Earthquake Spectra*, 24(4):997–1009.

Bommer, J. J., Scherbaum, F., Bungum, H., Cotton, F., Sabetta, F., and Abrahamson, N. A. (2005). On the use of logic trees for ground-motion prediction equations in seismic-hazard analysis. *Bulletin of the Seismological Society of America*, 95(2):377–389.

Boore, D. M. and Atkinson, G. M. (2008). Ground-motion prediction equations for

the average horizontal component of PGA, PGV, and 5%-damped PSA at spectral periods between 0.01 s and 10.0 s. *Earthquake Spectra*, 24(1):99–138.

Boore, D. M., Stewart, J. P., Seyhan, E., and Atkinson, G. M. (2014). NGA-West2 equations for predicting PGA, PGV, and 5% damped PSA for shallow crustal earthquakes. *Earthquake Spectra*, 30(3):1057–1085.

Bozorgnia, Y., Abrahamson, N. A., Atik, L. A., Ancheta, T. D., Atkinson, G. M., Baker, J. W., Baltay, A., Boore, D. M., Campbell, K. W., Chiou, B. S.-J., et al. (2014). NGA-West2 research project. *Earthquake Spectra*, 30(3):973–987.

Bradley, B. A. (2010). A generalized conditional intensity measure approach and holistic ground-motion selection. *Earthquake Engineering & Structural Dynamics*, 39(12):1321–1342.

Buratti, N., Stafford, P. J., and Bommer, J. J. (2010). Earthquake accelerogram selection and scaling procedures for estimating the distribution of drift response. *Journal of Structural Engineering*, 137(3):345–357.

Cabas, A., Rodriguez-Marek, A., and Bonilla, L. F. (2017). Estimation of site-specific kappa (κ_0)-consistent damping values at KiK-net sites to assess the discrepancy between laboratory-based damping models and observed attenuation (of seismic waves) in the field. *Bulletin of the Seismological Society of America*, 107(5):2258–2271.

Campbell, K. W. and Bozorgnia, Y. (2008). NGA ground motion model for the geometric mean horizontal component of PGA, PGV, PGD and 5% damped linear elastic response spectra for periods ranging from 0.01 to 10 s. *Earthquake Spectra*, 24(1):139–171.

Campbell, K. W. and Bozorgnia, Y. (2014). NGA-West2 ground motion model for the average horizontal components of PGA, PGV, and 5% damped linear acceleration response spectra. *Earthquake Spectra*, 30(3):1087–1115.

Canadian Commission on Building and Fire Codes (2015). National Building Code of Canada: 2015. Technical Report 0-660-03633-5, National Research Council of Canada. https://doi.org/10.4224/40002005.

Canadian Commission on Building and Fire Codes (2022). National Building Code of

Canada: 2020. Technical Report 0-660-37913-5, National Research Council of Canada. https://doi.org/10.4224/w324-hv93.

Chiou, B., Darragh, R., Gregor, N., and Silva, W. (2008). NGA project strong-motion database. *Earthquake Spectra*, 24(1):23–44.

Chiou, B.-J. and Youngs, R. R. (2008). An NGA model for the average horizontal component of peak ground motion and response spectra. *Earthquake Spectra*, 24(1):173–215.

Chiou, B. S.-J. and Youngs, R. R. (2014). Update of the Chiou and Youngs NGA model for the average horizontal component of peak ground motion and response spectra. *Earthquake Spectra*, 30(3):1117–1153.

Dawood, H. M., Rodriguez-Marek, A., Bayless, J., Goulet, C., and Thompson, E. (2016). A flatfile for the KiK-net database processed using an automated protocol. *Earthquake Spectra*, 32(2):1281–1302.

FEMA 273 (1997). NEHRP guidelines for the seismic rehabilitation of buildings. *Federal Emergency Management Agency*.

FEMA 356 (2000). Prestandard and commentary for the seismic rehabilitation of buildings. *Council and Building Seismic Safety, Federal Emergency Management Agency, Washington, DC*.

FEMA P695 (2009). Quantification of Building Seismic Performance Factors. *Applied Technology Council, Redwood City, California*.

Frohlich, C. (1992). Triangle diagrams: ternary graphs to display similarity and diversity of earthquake focal mechanisms. *Physics of the Earth and Planetary interiors*, 75(1-3):193–198.

García, D., Singh, S. K., Herráiz, M., Ordaz, M., and Pacheco, J. F. (2005). Inslab earthquakes of central Mexico: peak ground-motion parameters and response spectra. *Bulletin of the Seismological Society of America*, 95(6):2272–2282.

Garcia, D., Wald, D. J., and Hearne, M. (2012). A global earthquake discrimination scheme to optimize ground-motion prediction equation selection. *Bulletin of the Seismological Society of America*, 102(1):185–203.

GEM (2022). The OpenQuake-engine User Manual. *Global Earthquake Model. OpenQuake Manual for Engine version 3.13.0*.

Ghofrani, H. and Atkinson, G. M. (2014). Ground-motion prediction equations for interface earthquakes of M7 to M9 based on empirical data from Japan. *Bulletin of earthquake engineering*, 12(2):549–571.

Goda, K. (2019). Nationwide earthquake risk model for wood-frame houses in Canada. *Frontiers in Built Environment*, 5:128.

Goda, K. and Atkinson, G. M. (2009). Probabilistic characterization of spatially correlated response spectra for earthquakes in Japan. *Bulletin of the Seismological Society of America*, 99(5):3003–3020.

Goda, K. and Sharipov, A. (2021). Fault-source-based probabilistic seismic hazard and risk analysis for Victoria, British Columbia, Canada: A case of the Leech River Valley fault and Devil's Mountain fault system. *Sustainability*, 13(3):1440.

Goda, K., Wenzel, F., and De Risi, R. (2015). Empirical assessment of non-linear seismic demand of mainshock–aftershock ground-motion sequences for Japanese earthquakes. *Frontiers in built environment*, 1:6.

Gutenberg, B. and Richter, C. F. (1944). Frequency of earthquakes in California. *Bulletin of the Seismological Society of America*, 34(4):185–188.

Halchuk, S., Allen, T., Adams, J., and Onur, T. (2019). Contribution of the Leech River Valley-Devil's Mountain Fault System to Seismic Hazard in Victoria, BC. In *12th Canadian Conference on Earthquake Engineering*.

Haselton, C. B., Fry, A., Baker, J. W., Hamburger, R. O., Whittaker, A. S., Stewart, J. P., Elwood, K. J., Luco, N., Hooper, J. D., Charney, F. A., et al. (2014). A fully revised chapter 16 methodology proposed for the 2015 NEHRP Provisions and the ASCE/SEI 7-16 Standard. In *10th US National conference on earthquake engineering. Anchorage, Alaska, USA*.

Haselton, C. B., Liel, A. B., Deierlein, G. G., Dean, B. S., and Chou, J. H. (2011). Seismic collapse safety of reinforced concrete buildings. i: Assessment of ductile moment frames. *Journal of Structural Engineering*, 137(4):481–491.

Ibarra, L. F., Medina, R. A., and Krawinkler, H. (2005). Hysteretic models that

incorporate strength and stiffness deterioration. *Earthquake engineering & structural dynamics*, 34(12):1489–1511.

Inoue, T. and Cornell, C. A. (1990). Seismic hazard analysis of multi-degree-of-freedom structures. report no. RMS-8.

Jayaram, N. and Baker, J. W. (2008). Statistical tests of the joint distribution of spectral acceleration values. *Bulletin of the Seismological Society of America*, 98(5):2231–2243.

Jayaram, N., Lin, T., and Baker, J. W. (2011). A computationally efficient ground-motion selection algorithm for matching a target response spectrum mean and variance. *Earthquake Spectra*, 27(3):797–815.

Johnson, R. A., Wichern, D. W., et al. (2002). *Applied multivariate statistical analysis*, volume 5/8. Prentice hall Upper Saddle River, NJ.

Kagan, Y. Y. (2002). Seismic moment distribution revisited: I. Statistical results. *Geophysical Journal International*, 148(3):520–541.

Kolaj, M., Adams, J., and Halchuk, S. (2020a). The 6th Generation seismic hazard model of Canada. In *17th World Conference on Earthquake Engineering, Sendai, Japan, Paper 1c-0028*.

Kolaj, M., Allen, T., Mayfield, R., Adams, J., and Halchuk, S. (2019). Ground-motion models for the 6th generation seismic hazard model of Canada. In *12th Canadian Conference on Earthquake Engineering*.

Kolaj, M., Halchuk, S., Adams, J., and Allen, T. (2020b). Sixth generation seismic hazard model of Canada: input files to produce values proposed for the 2020 National Building Code of Canada. Technical report, Geological Survey of Canada. Open File 8630, https://doi.org/10.4095/327322.

Kramer, S. L. (1996). *Geotechnical Earthquake Engineering*, volume 80. Prentice Hall Upper Saddle River, NJ.

Liel, A. B., Haselton, C. B., Deierlein, G. G., and Baker, J. W. (2009). Incorporating modeling uncertainties in the assessment of seismic collapse risk of buildings. *Structural safety*, 31(2):197–211.

Lignos, D. G. and Krawinkler, H. (2011). Deterioration modeling of steel components in

support of collapse prediction of steel moment frames under earthquake loading. *Journal of Structural Engineering*, 137(11):1291–1302.

Luco, N. and Bazzurro, P. (2007). Does amplitude scaling of ground motion records result in biased nonlinear structural drift responses? *Earthquake Engineering & Structural Dynamics*, 36(13):1813–1835.

McGuire, R. K. (1995). Probabilistic seismic hazard analysis and design earthquakes: closing the loop. *Bulletin of the Seismological Society of America*, 85(5):1275–1284.

NIED (2019). K-NET, KiK-net, National Research Institute for Earth Science and Disaster Resilience. https://dx.doi.org/10.17598/nied.0004.

Noh, N. M., Liberatore, L., Mollaioli, F., and Tesfamariam, S. (2017). Modelling of masonry infilled RC frames subjected to cyclic loads: State of the art review and modelling with OpenSees. *Engineering Structures*, 150:599–621.

NRCC (2015). Structural commentaries (user's guide—NBC 2015: Part 4 of division B).

Odikamnoro, I., Badal, P. S., Burton, H., and Tesfamariam, S. (2022). Seismic collapse risk of RC-timber hybrid building with different energy dissipation connections considering NBCC 2020 hazard. *Journal of Infrastructure Preservation and Resilience*, 3(1):1–13.

Okada, Y., Kasahara, K., Hori, S., Obara, K., Sekiguchi, S., Fujiwara, H., and Yamamoto, A. (2004). Recent progress of seismic observation networks in Japan—Hi-net, F-net, K-NET and KiK-net. *Earth, Planets and Space*, 56(8):xv–xxviii.

Pilz, M. and Cotton, F. (2019). Does the one-dimensional assumption hold for site response analysis? A study of seismic site responses and implication for ground motion assessment using KiK-Net strong-motion data. *Earthquake Spectra*, 35(2):883–905.

Power, M., Chiou, B., Abrahamson, N., Bozorgnia, Y., Shantz, T., and Roblee, C. (2008). An overview of the NGA project. *Earthquake spectra*, 24(1):3–21.

Runge, A. and Scherbaum, F. (2012). The quantification of consistent subjective logic

tree branch weights for PSHA. In *EGU General Assembly Conference Abstracts*, page 7806.

Scherbaum, F. and Kuehn, N. M. (2011). Logic tree branch weights and probabilities: Summing up to one is not enough. *Earthquake Spectra*, 27(4):1237–1251.

Tesfamariam, S. and Goda, K. (2015). Loss estimation for non-ductile reinforced concrete building in Victoria, British Columbia, Canada: effects of mega-thrust Mw9-class subduction earthquakes and aftershocks. *Earthquake Engineering & Structural Dynamics*, 44(13):2303–2320.

Tesfamariam, S., Skandalos, K., Goda, K., Bezabeh, M. A., Bitsuamlak, G., and Popovski, M. (2021). Quantifying the Ductility-Related Force Modification Factor for 10-Story Timber-RC Hybrid Building Using FEMA P695 Procedure and Considering the 2015 NBC Seismic Hazard. *Journal of Structural Engineering*, 147(5):04021052.

Tremblay, R., Atkinson, G. M., Bouaanani, N., Daneshvar, P., Léger, P., and Koboevic, S. (2015). Selection and scaling of ground motion time histories for seismic analysis using NBCC 2015. In *11th Canadian Conference on Earthquake Engineering (11CCEE), Victoria, BC, Canada*, volume 99060.

Vamvatsikos, D. and Cornell, C. A. (2002). Incremental dynamic analysis. *Earthquake engineering & structural dynamics*, 31(3):491–514.

Watson-Lamprey, J. and Abrahamson, N. (2006). Selection of ground motion time series and limits on scaling. *Soil Dynamics and Earthquake Engineering*, 26(5):477–482.

Wells, D. L. and Coppersmith, K. J. (1994). New empirical relationships among magnitude, rupture length, rupture width, rupture area, and surface displacement. *Bulletin of the Seismological Society of America*, 84(4):974–1002.

Zhao, J. X., Zhang, J., Asano, A., Ohno, Y., Oouchi, T., Takahashi, T., Ogawa, H., Irikura, K., Thio, H. K., Somerville, P. G., et al. (2006). Attenuation relations of strong ground motion in Japan using site classification based on predominant period. *Bulletin of the Seismological Society of America*, 96(3):898–913.

Zhao, J. X., Zhou, S., Gao, P., Long, T., Zhang, Y., Thio, H. K., Lu, M., and Rhoades, D. A. (2015). An earthquake classification scheme adapted for Japan determined

by the goodness of fit for ground-motion prediction equations. *Bulletin of the Seismological Society of America*, 105(5):2750–2763.

Zhu, C., Weatherill, G., Cotton, F., Pilz, M., Kwak, D. Y., and Kawase, H. (2021). An open-source site database of strong-motion stations in Japan: K-NET and KiK-net (v1. 0.0). *Earthquake Spectra*, 37(3):2126–2149.